creative commons
COMMONS DEED

저작자표시-비영리-변경금지 2.0 대한민국

이용자는 아래의 조건을 따르는 경우에 한하여 자유롭게

- 이 저작물을 복제, 배포, 전송, 전시, 공연 및 방송할 수 있습니다.

다음과 같은 조건을 따라야 합니다:

저작자표시. 귀하는 원저작자를 표시하여야 합니다.

비영리. 귀하는 이 저작물을 영리 목적으로 이용할 수 없습니다.

변경금지. 귀하는 이 저작물을 개작, 변형 또는 가공할 수 없습니다.

- 귀하는, 이 저작물의 재이용이나 배포의 경우, 이 저작물에 적용된 이용허락조건을 명확하게 나타내어야 합니다.
- 저작권자로부터 별도의 허가를 받으면 이러한 조건들은 적용되지 않습니다.

저작권법에 따른 이용자의 권리는 위의 내용에 의하여 영향을 받지 않습니다.

이것은 이용허락규약(Legal Code)을 이해하기 쉽게 요약한 것입니다.

Disclaimer

dCollection

이학석사학위논문

Search for a Light Charged Higgs Decaying into $c\bar{b}$ in the CMS experiment with pp collisions at $\sqrt{s}=8$ TeV

CMS 실험의 8 TeV 에너지의 양성자 충돌에서 Light Charged Higgs의 $c\bar{b}$ 붕괴모드 탐색

2016년 8월

서울대학교 대학원

물리천문학부

좌 연 재

Search for a Light Charged Higgs Decaying into $c\bar{b}$ in the CMS experiment with pp collisions at $\sqrt{s}=8$ TeV

CMS 실험의 8 TeV 에너지의 양성자 충돌에서 Light Charged Higgs의 $c\bar{b}$ 붕괴모드 탐색

지도교수 양 운 기

이 논문을 이학석사 학위논문으로 제출함

2016년 8월

서울대학교 대학원

물리천문학부

좌 연 재

좌연재의 이학석사 학위논문을 인준함

2016년 6월

위 원 장 최 선 호 (인)

부위원장 양 운 기 (인)

위 원 유 휘 동 (인)

Search for a Light Charged Higgs Decaying into $c\bar{b}$ in the CMS experiment with pp collisions at $\sqrt{s}=8$ TeV

Yeon-jae Jwa

supervised by
Professor Un-ki Yang

A Dissertation
Submitted to the Faculty of
Seoul National University
in Partial Fulfillment of
the Requirements for the Degree of
Master of Philosophy

June 2016

Department of Physics and Astronomy
Graduate School
Seoul National University

Search for a Light Charged Higgs Decaying into cbbar in the CMS experiment with pp collisions at $\sqrt{s} = 8$ TeV

-

2016 6

Search for a Light Charged Higgs Decaying into cbbar in the CMS experiment with pp collisions at $\sqrt{s} = 8$ TeV

2016 6

2016 6

_____()

_____ ()

_____ ()

_____ ()

_____ ()

Search for a Light Charged Higgs Decaying into cbbar in the CMS experiment with pp collisions at $\sqrt{s} = 8$ TeV

Yeon-jae Jwa

Supervised by

Professor **Un-ki Yang**

A Dissertation

Submitted to the Faculty of

Seoul National University

in Partial Fulfillment of

the Requirements for the Degree of

Master of Science

June 2016

Department of Physics and Astronomy

Graduate School

Seoul National University

Abstract

This document describes the first attempt to search for a charged Higgs boson decaying to $c\bar{b}$ in top quark events in a CMS data corresponding to 19.7 fb^{-1} at $\sqrt{s} = 8$ TeV in LHC. The $t\bar{t}$ event in lepton+jets channel consists of a lepton, missing transverse energy, two b-jets, and two light quark jets in the final state. If a charged Higgs is produced in place of the hadronic W and it decays to $c\bar{b}$, one more b-jet will be found in the final state. Selected $t\bar{t}$ events are thrown to a kinematic fitter for the full reconstruction constraining both leptonic and hadronic top quark mass, and leptonic W to their PDG values. The di-jet invariant mass is the only free parameter and reveals W mass from the SM $t\bar{t}$ events. This analysis looks for an excess over the hadronic W in the di-jet mass distribution in two b-tagged and three b-tagged events simultaneously. Upper limits on the branching ratio of a top quark decaying to a charged Higgs and b quark with 95% C.L. are placed at $\sim 1\%$ for $H^{\pm}$ mass of 90 to 150 GeV/c^2 in null hypothesis.

Keywords: Charged Higgs, Two Higgs Doublet Models, Multi Higgs Doublet Models

Student Number: 2014-21375

Contents

Abstract **vii**

1 Introduction **1**

1.1 The Standard Model 1

1.2 Extra Higgs boson 3

1.2.1 Beyond Standard Model Higgs Sector 3

1.2.2 Charged Higgs Boson 5

2 Large Hadron Collider and CMS detector **6**

2.1 Large Hadron Collider 6

2.2 Compact Muon Solenoid 8

2.2.1 Coordinate Convention 10

2.2.2 Superconducting Solenoid 11

2.2.3 Tracking Detectors 11

2.2.4 Caloriemeter Subdetectors 11

2.2.5 Muon Detectors 12

2.2.6 Trigger 12

3 Data and Simulated Sample **14**

3.1 Simulation Samples 15

3.2 Data samples and Trigger 15

4 Event Selection **18**

4.1 Object Identification and Selection 18

4.1.1 Pre-selection cuts 21

4.1.2 Data driven QCD sample 24

4.2 Treatment on two or more b-tagged Sample 25

4.3 Event Yields and Control Region Plots 26

5 Top Specific Correction **35**

5.1 Top Specific Correction Performance 41

6 $t\bar{t}$ Event Reconstruction **43**

6.1 Kinematic fitter 43

6.2 Goodness Cut 45

6.3 High $H^{\pm}$ mass fitter 48

6.4 Kinematic Fitter Performance 52

6.5 Mass Template 56

7 Systematic Uncertainty **60**

8 Fit on B($t \to H^{\pm}b$) **75**

8.1 Upper limit on B($t \to H^{\pm}b$) at 95% CL with Stat. Error 75

8.2 Upper limit on B($t \to H^{\pm}b$) at 95% CL with Syst. Error 76

9 Result and Summary **80**

A Appendix **87**

A.1 Measurements of Jet Response and its Uncertainty 87

A.2 Mass Templates: $H^{\pm}$ vs $W^{\pm}$ in $t\bar{t}$ 88

Abstract in Korean **97**

List of Figures

1.1 Elementary Particles of the Standard Model 2

1.2 Branching ratio of $H^{\pm}$ decay channels as a function of the M($H^{\pm}$) 4

2.1 LHC complex 7

2.2 Overview of the Compact Muon Solenoid 9

2.3 Transverse view of a slice of the CMS detector 10

4.1 Plots in 1 b-tag region. Upper left plot: number of vertices for e+jets channel, upper right plot: number of vertices for μ+jets channel, bottom left plot: jet multiplicity for e+jets channel, bottom right plot: jet multiplicity for μ+jets channel. 22

4.2 Normalized number of b-jets in the SM $t\bar{t}$ sample (light blue filled) compared with the $H^{\pm}$ signal $t\bar{t}$ sample (colored lines). . . 23

4.3 Lepton relative isolation in 1b-tagging region 25

4.4 Control plots in 1b-tagging region: jet multiplicity, MET 28

4.5 Control region: p_T distributions of e(left)/μ(right) and four jets in order. 29

4.6 Control region: η distributions of e(left)/μ(right) and four jets in order. 30

4.7 Signal Region: p_T distributions of lepton+4jets in 2 b-tags region. 31
4.8 Signal Region: η distributions of lepton+4jets in 2 b-tags region. 32
4.9 Signal Region: p_T distributions of lepton+4jets in 3 b-tags region. 33
4.10 Signal Region: η distributions of lepton+4jets in 3 b-tags region. 34

5.1 Jet p_T responses as a function of reconstructed p_T for a b-quark jet, c-quark jet, and light-flavour jet where $|\eta|$ is smaller than 0.174 37
5.2 Corrected p_T response distributions for b-quark jet in p_T bins . 38
5.3 Corrected p_T response distributions for b-quark jet in η bins . . 39
5.4 Parametric fit of the TS correction uncertainty of b-quark jet as a function of p_T in nine different η region 40
5.5 Di-jet invariant mass before/after the TS correction 41
5.6 Hadronic top mass reconstruction before/after TS correction . . 42

6.1 Di-jet invariant mass reconstruction by the kinematic fit 46
6.2 p_T difference distribution for jets in SM $t\bar{t}$ events 47
6.3 Hadronic side top quark mass distributions for right/wrong assignment of jets 48
6.4 Di-jet invariant mass with the goodness cuts 49
6.5 p_T distribution of the top-b-parton in the hadronic side top quark 50
6.6 Di-jet mass distribution in the three b-tagged jets events with normal fitter and high mass fitter 51

6.7 Mass reconstruction with kinematic fitter input jets (left), mass reconstruction with kinematic fitter output jets (right) in ≥ 3 b-jets events 52
6.8 Mass reconstruction with kinematic fitter input jets (left), mass reconstruction with kinematic fitter output jets (right) in ≥ 3 b-jets events 53
6.9 Mass reconstruction with high mass kinematic fitter input jets (left), mass reconstruction with high mass kinematic fitter output jets (right) in ≥ 3 b-jets events 54
6.10 Mass reconstruction with high mass kinematic fitter input jets (left), mass reconstruction with high mass kinematic fitter output jets (right) in ≥ 3 b-jets events 55
6.11 Di-jet mass distribution MC background stack in the two b-tagged jets events in e+jets(left) and μ+jets(right) channel . . . 57
6.12 Di-jet mass distribution MC background stack in the three b-tagged jets events in e+jets(left) and μ+jets(right) channel with the normal fitter 58
6.13 Di-jet mass distribution MC background stack in the three b-tagged jets events in e+jets(left) and μ+jets(right) channel with the high mass fitter 59

7.1 Systematic uncertainties for di-jet mass reconstruction of the Standard Model $t\bar{t}$ (left), and for charged Higgs signal at 100 GeV/c^2 (right) in 3 b-tags e+jets channel for low mass fitter: showing shape uncertainties due to jet energy scale, jet energy resolution, L5 b-quark uncertainty, and L5 other flavored quark uncertainty from top plots toward bottom plots 67

7.2 $t\bar{t}$ Systematic uncertainties for di-jet mass reconstruction of the Standard Model $t\bar{t}$ (left) in 3 b-tag e+jets channel for low mass fitter, showing shape uncertainties due to MC generator, top quark mass, Q^2 scale, ME-matching, and p_T-reweight for $t\bar{t}$ and $H^{\pm}$ (100 GeV/c^2) from top plots toward the bottom plots. . . . 68

7.3 Systematic uncertainties for di-jet mass reconstruction of the Standard Model $t\bar{t}$ with high mass fitter(left) and of charged Higgs signal at 130 GeV/c^2 with high mass fitter(right) in 3 b-tag e+jets channel, jet energy scale, jet energy resolution, L5 b-quark uncertainty, and L5 other flavored quark uncertainty from top plots toward the bottom plots 69

7.4 $t\bar{t}$ Systematic uncertainties for di-jet mass reconstruction of the Standard Model $t\bar{t}$ (left) in 3 b-tag e+jets channel for high mass fitter, showing shape uncertainties due to MC generator, top quark mass, Q^2 scale, ME-matching, and p_T-reweight for $t\bar{t}$ and $H^{\pm}$ (130 GeV/c^2) from top plots toward the bottom plots. . . . 70

7.5 Systematic uncertainties for di-jet mass reconstruction of the Standard Model $t\bar{t}$ (left) and for charged Higgs signal at 100 GeV/c^2 (right) in 3 b-tags e+jets channel for low mass fitter: template shifts due to jet energy scale, jet energy resolution, L5 b-quark uncertainty, and L5 other flavored quark uncertainty from top plots toward the bottom plots. 71

7.6 $t\bar{t}$ Systematic uncertainties for di-jet mass reconstruction of the Standard Model $t\bar{t}$ (left) in 3 b-tag e+jets channel for low mass fitter, showing shape uncertainties due to MC generator, top quark mass, Q^2 scale, ME-matching, and p_T-reweight for $t\bar{t}$ and $H^{\pm}$ (100 GeV/c^2) from top plots toward the bottom plots. . . . 72

7.7 Systematic uncertainties for di-jet mass reconstruction of the Standard Model $t\bar{t}$ with high mass fitter(left) and of charged Higgs signal at 130 GeV/c^2 with high mass fitter(right) in 3 b-tag e+jets channel, jet energy scale, jet energy resolution, L5 b-quark uncertainty, and L5 other flavored quark uncertainty from top plots toward the bottom plots 73

7.8 $t\bar{t}$ Systematic uncertainties for di-jet mass reconstruction of the Standard Model $t\bar{t}$ (left) in 3 b-tag e+jets channel for high mass fitter, showing shape uncertainties due to MC generator, top quark mass, Q^2 scale, ME-matching, and p_T-reweight for $t\bar{t}$ and $H^{\pm}$ (130 GeV/c^2) from top plots toward the bottom plots. . . . 74

8.1 Upper limit on B($t \to H^{\pm}b$) with 95% C.L. for electron channel, 2 b-tags (left) and 3 b-tags (right) template fit respectively. No systematic uncertainty included. 76
8.2 Upper limit on B($t \to H^{\pm}b$) with 95% C.L. for muon channel, 2 b-tags (left) and 3 b-tags (right) template fit respectively. No systematic uncertainty included. 77
8.3 Upper limit on B($t \to H^{\pm}b$) with 95% C.L. for combined (2 b-tags & 3 b-tags) fit for muon (left) and electron channel (right) respectively. No systematic uncertainty included. 77
8.4 Upper limit on B($t \to H^{\pm}b$) with 95% C.L. for electron channel, 2 b-tags (left) and 3 b-tags (right) template fit respectively. All systematic uncertainties included. 78
8.5 Upper limit on B($t \to H^{\pm}b$) with 95% C.L. for muon channel, 2 b-tags (left) and 3 b-tags (right) template fit respectively. All systematic uncertainties included. 78
8.6 Upper limit on B($t \to H^{\pm}b$) with 95% C.L. for combined (2 b-tags & 3 b-tags) fit for muon (left) and electron channel (right) respectively. All systematic uncertainties included. 79

9.1 Upper limit on B($t \to H^{\pm}b$) with 95% C.L. in combination of electron and muon channel. Limit with statistical uncertainty only seen on left and the limit with all systematic uncertainties shown on right. 81

9.2 Upper limit on B($t \to H^{\pm}b$) with 95% C.L. for combined (2 b-tags & 3 b-tags) fit for muon (left) and electron channel (right) respectively. All systematic uncertainties included. The result from data is overlaid. 81
9.3 Upper limit on B($t \to H^{\pm}b$) with 95% C.L. in combination of electron and muon channel. The result from data is overlaid. . . 82

A.1 Corrected pT response distributions for c-quark jet where $|\eta|$ is smaller than 0.174 89
A.2 Corrected pT response distributions for light-flavour jet where $|\eta|$ is smaller than 0.174 90
A.3 Corrected pT response distributions for c-quark jet where jet pT is between 100 GeV/c^2 to 120 GeV/c^2. 91
A.4 Corrected pT response distributions for light-flavour jet where jet pT is between 100 GeV/c^2 to 120 GeV/c^2. 92
A.5 Parameter fitting of correction uncertainty of c-quark jet with a function of pT in each η region 93
A.6 Parameter fitting of correction uncertainty of light-flavour jet with a function of pT in each η region 94
A.7 Low Mass Templates in 3b-tags: $H^{\pm}$ vs W for $H^{\pm}$ mass of 90 to 120 GeV/c^2 with a normalization to unity. Template for e+jets on left and μ+jets on right side. 95

A.8 High Mass Templates in 3b-tags: $H^{\pm}$ vs W for $H^{\pm}$ mass of 130 to 150 GeV/c^2 with a normalization to unity. Template for e+jets on left and μ+jets on right side. 96

List of Tables

3.1 List of simulation samples of SM background processes 16

3.2 List of simulation samples of $t\bar{t}$ systematic uncertainties. Effective luminosities are calculated using the $\sigma_{t\bar{t}} = 252.89$ pb. 17

3.3 List of CMS datasets for pp collisions at $\sqrt{s} = 8$ TeV 17

4.1 QCD scale factors for e+jets and μ+jets channel 25

4.2 Event yields with the e+jets selection from MC samples and data corresponding to 19.7 fb^{-1} at $\sqrt{s} = 8$ TeV 26

4.3 Event yields with the μ+jets selection from MC samples and data corresponding to 19.7 fb^{-1} at $\sqrt{s} = 8$ TeV 27

7.1 List of rate systematic uncertainties of e+jets channel $H^{\pm}$ signal samples 2b-tags 65

7.2 List of rate systematic uncertainties of e+jets channel $H^{\pm}$ signal samples 3b-tags 65

7.3 List of rate systematic uncertainties of e+jets channel $t\bar{t}$ sample 65

7.4 List of rate systematic uncertainties of e+jets channel non-$t\bar{t}$ samples 65

7.5 List of rate systematic uncertainties of μ+jets channel $H^{\pm}$ signal samples 2b-tags 66
7.6 List of rate systematic uncertainties of μ+jets channel $H^{\pm}$ signal samples 3b-tags 66
7.7 List of rate systematic uncertainties of μ+jets channel $t\bar{t}$ sample 66
7.8 List of rate systematic uncertainties of μ+jets channel non-$t\bar{t}$ samples 66

Chapter 1

Introduction

1.1 The Standard Model

In particle physics, we try to understand the world as a composition of elementary particles. The Standard Model with a dozen fermions and gauge bosons shares the same point of view. The Standard Model is the mostly accepted theory in current particle physics, and many experimental results including the recent Higgs boson discovery can be explained by the Standard Model. In the Standard Model, physical phenomena appear due to the interactions between elementary particles.

Fig.1.1 shows the elementary particles and gauge bosons consisting the Standard Model. The twelve elementary particles can be separated by two groups of particles; quarks and leptons. Six particles are called quarks and other six particles are called leptons. Quarks and leptons are fermions with spin 1/2. There are three generations where one generation contains two leptons(one charged lepton and one neutrino) and two quarks. There interactions are performed by exchanging field quanta and each interaction has their as-

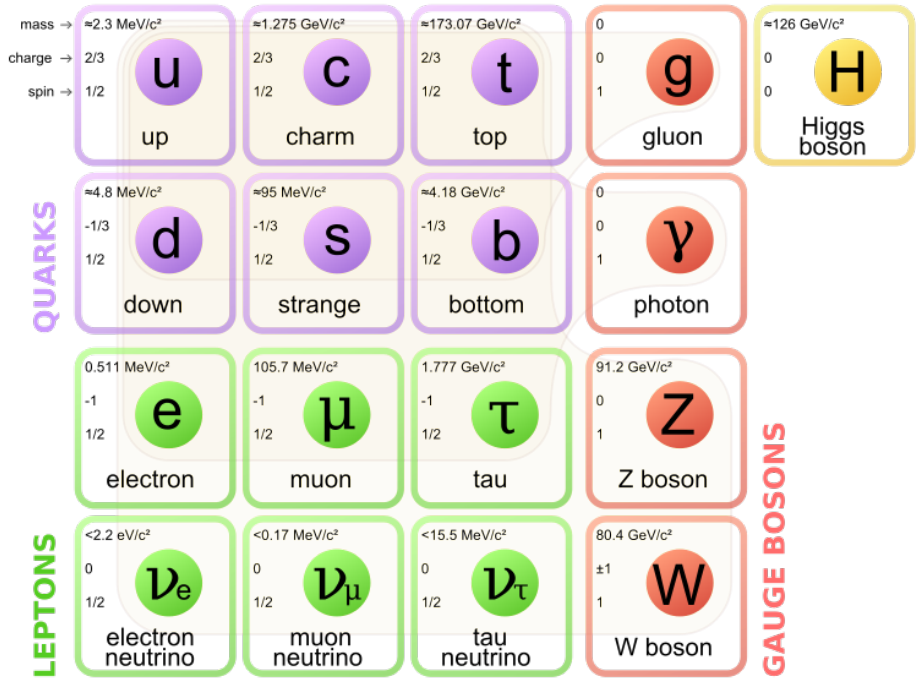

Figure 1.1: Elementary Particles of the Standard Model

sociated force carrying particle. The EM interaction, which is the interaction between charged particles, is mediated by the exchange of massless gauge boson; photon. The quantum field theory for the EM interaction is called the QED(quantum electrodynamics). The QED uses Lagrangian formalism in extracting the equation of motion of electrically charged particles. The massive gauge bosons (W+, W-, and Z) mediate weak interaction between all quarks and leptons. The quarks which have colour charge go through the strong interaction mediated by massless gluon. Where the EM and Weak interactions are understood as a Electroweak interaction, Electroweak gauge bosons can

have mass through breaking SU(2)U(1) symmetry by Spontaneous Symmetry Breaking mechanism. The mass generation of W+, W-, and Z bosons by electroweak symmetry breaking is referred as "Higgs mechanism".

For Higgs mechanism, Higgs field should exist, and theorists and experimentalist had looked for the Higgs boson for decades. Being the last puzzle piece of the Standard Model, the Higgs boson has a significant implication. And Finally, the CMS and ATLAS experiments in Large Hadron Collider declared the discovery of the Higgs boson in 2012 [8, 16] and the discovered particle is confirmed to be neutral scalar particle in 2013 [10, 18]. Also the Higgs boson is found to be in correspondence with the Standard Model predictions [2, 27, 28, 30].

1.2 Extra Higgs boson

1.2.1 Beyond Standard Model Higgs Sector

The Standard Model, though it is the most spread and accepted theory in particle physics, has its limit. For example, the Standard Model does not give an answer to the Higgs mass hierarchy problem. More precisely, Higgs mass at 125GeV means that the quadratic radiative corrections and Higgs bare mass should make a fine-tuning cancellation, because otherwise the Higgs boson mass would be huge 10^{16} GeV due to the large quantum contributions. There have been attempts to resolve the Higgs mass problem by introducing extended Higgs sector, while the Minimal Standard Model allows only one Higgs doublet to explain spontaneous symmetry breaking. If we allow more

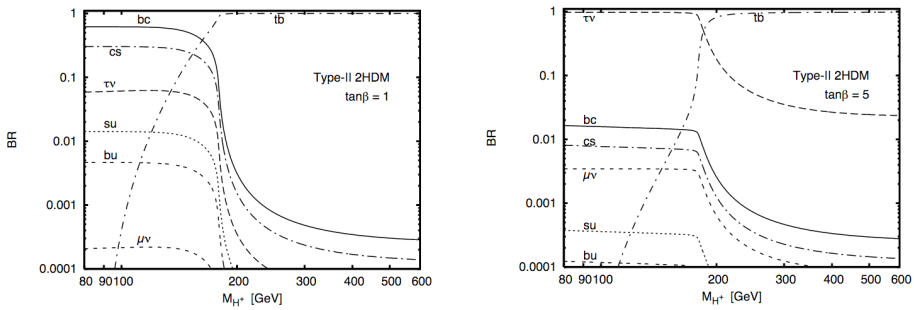

Figure 1.2: Branching ratio of $H^{\pm}$ decay channels as a function of the M($H^{\pm}$) assuming tanβ=5(left), 10(right), quoted from [21].

Higgs doublets, we earns more Higgs fields. When there are two Higgs doublets, these models are called 2HDMs(Two Higgs Doublet Models) and if there are more than two Higgs doublets, these models are called MHDMs(Multi Higgs Doublet Models). If the nature chooses two Higgs doublets (two Higgs doublet model, 2HDM) [23], there appear two charged ($H^{\pm}$) and three neutral Higgs bosons(A, H, h), and the observed Higgs boson can be considered as one of the CP-even neutral bosons (H or h).

1.2.2 Charged Higgs Boson

Charged Higgs bosons have either +1 or -1 electric charge. Several expected charged Higgs decay products are tau and neutrino, charm quark and strange quark, and charm quark and bottom quark. In a generic 2HDM, there are two $SU(2)_L$ doublet scalar fields ϕ_1 and ϕ_2. Depending on which type of fermions couples to which doublet Φ, one can divide two-Higgs-doublet models into four different classes(type-I, type-II, type-X and type-Y). and the branching ratios of charged Higgs decay channels vary by these types and $tan\beta$ (where $tan\beta =$ the ratio of the vacuum expectation values of ϕ_1 and ϕ_2). In particular, the branching ratio of charged Higgs to cb-bar can be dominant in type-Y 2HDM. Moreover, the branching ratio for the decay $H^{\pm} \rightarrow$ cb can be as large as 80% in the Aligned Two Higgs Doublet Model(2HDM with aligned Yukawa sector) and in models with three or more Higgs doublets [29]. With the LHC first run, searches of charged Higgs to $\tau\nu$ [1, 9, 12, 26, 33], cs [11, 13, 20, 32] have been performed by both CMS and ATLAS collaboration. The branching ratio limit for the hadronic decaying channel($H^{\pm} \rightarrow$ cs) is observed to be 1.2 to 6.5% ranging the charged Higgs mass from 90 GeV to 150 GeV with the CMS run1 result [32]. There is no public result for charged Higgs to cb channel, and this document reports the search of light charged Higgs by $H^{\pm} \rightarrow$ cb decay channel.

Chapter 2

Large Hadron Collider and CMS detector

2.1 Large Hadron Collider

The Large Hadron Collider (LHC) is the world's largest and most energetic particle collider, the most complicated experimental facility ever built. It was constructed by the European Organization for Nuclear Research (CERN) from 1998 to 2008 in collaboration with over 10,000 scientists and engineers from over 100 countries, and hundreds of universities and laboratories.

The size of the tunnel which LHC lies in, is 27 kilometres in circumference and is located 175 meters underground beneath the France-Switzerland border near Geneva, Switzerland. The first research run at the LHC from March 2010 was at an initial energy of 3.5 TeV for each proton beam and the energy rose to 4 TeV for each beam from 2012 to February 2013. From then, it was shut down for upgrades and the beam energy went up to 6.5 TeV from May 2015. In 2016, it is scheduled to have 6.5 TeV beam as well. The goal of the LHC

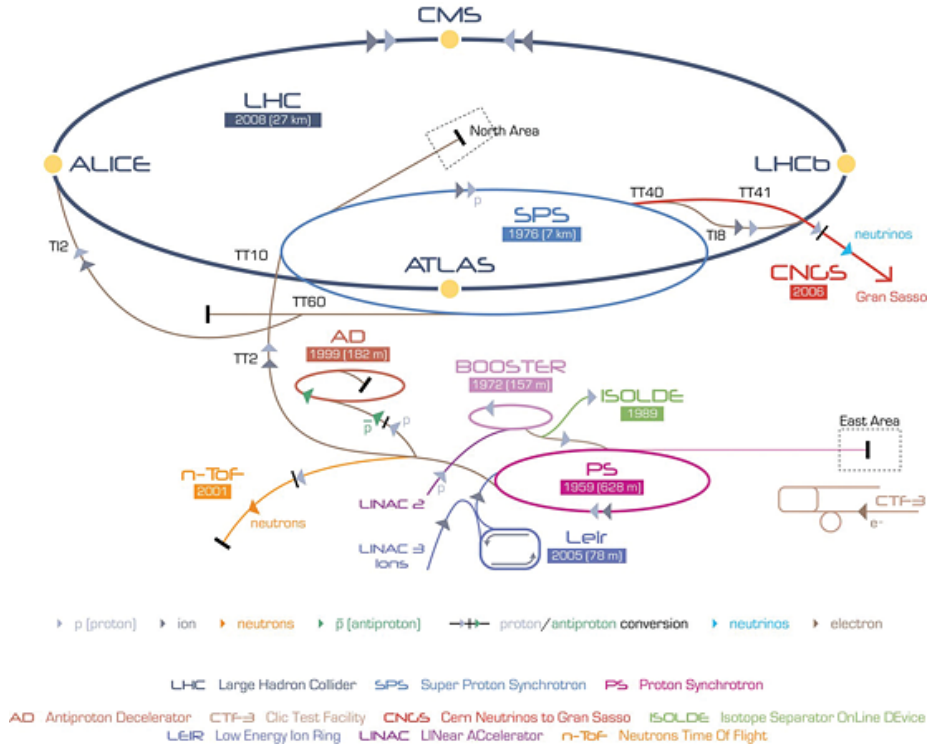

Figure 2.1: LHC complex

is to allow physicists to test the many theoretical predictions of high-energy particle physics. In general, it is aimed to further test the Beyond Standard Model(BSM) scenarios as well as test the properties of the Higgs boson and make measurements on the Standard Model processes.

The LHC contains seven detectors, each of them are designed for certain purpose. All of the seven detectors are located underground in large caverns excavated at the LHC's intersection points. Two of them, the ATLAS experiment and the Compact Muon Solenoid (CMS), are large, general purpose particle detectors. ALICE and LHCb have more specific roles and the last

three, TOTEM, MoEDAL and LHCf, are very much smaller and are for very specialized research. The proton-proton collision is the main collision at the LHC, but the proton-lead and lead-lead collisions are also being performed.

The LHC's computing grid is worldly notable. Approximately 15 petabytes of data is produced by LHC per year and the LHC Computing Grid was built to handle the large amounts of data.

One of the prior goals of the LHC was to seek for the possible existence of the Higgs boson, which had been predicted by theory for long but yet discovered before the LHC. During the first run of the LHC the Higgs boson discovery was announced. On 4 July 2012, both the CMS and ATLAS teams declared the discovery of a boson in the mass region around 125 GeV/c^2, with a statistical significance at the level of 5 sigma each. The observed properties were consistent with the Standard Model predictions for Higgs boson.

2.2 Compact Muon Solenoid

The Compact Muon Solenoid (CMS) detector is a general purpose detector built at the LHC interaction point 5 (P5). The CMS detector consists of silicon tracking system, an electromagnetic and hadron calorimeter, and a muon system and superconducting solenoid magnet provides a magnetic field of 3.8 T. The CMS detector is 22 m long, has a diameter of 15 m, and it weighs 14×10^3 tons overall. Fig.2.2 presents an exploded view of the CMS detector.

A particle emerging from a proton-proton collision will first meet the tracking system(silicon pixels and silicon strip detectors). The tracking system mea-

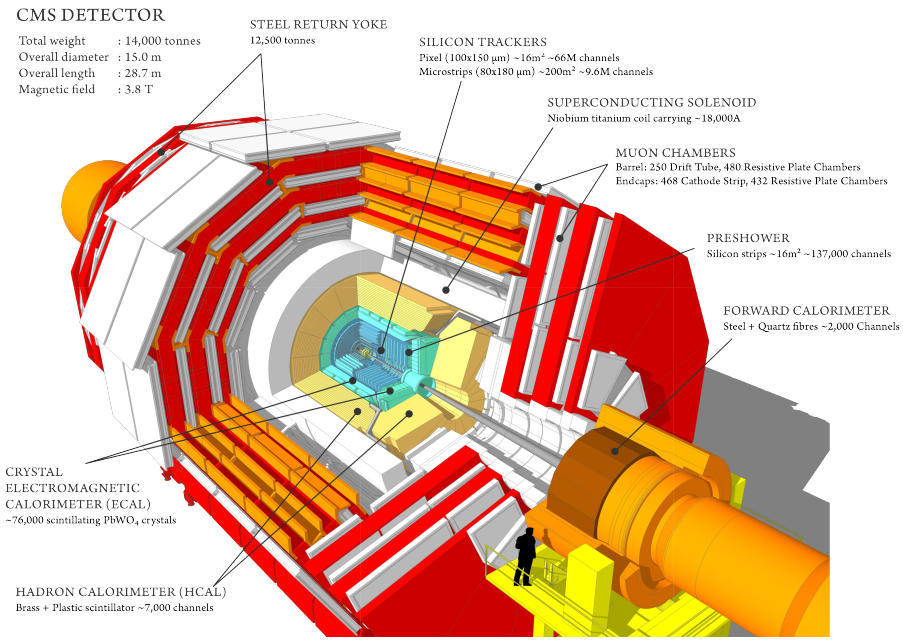

Figure 2.2: Overview of the Compact Muon Solenoid

sures the position of charged particles, these position information can reconstruct particle trajectories. The trajectories of these charged particles have curvature under the magnetic field, so that one can calculate their momenta. The first calorimeter layer, called the electromagnetic calorimeter(ECAL), measures the energies of electrons and photons with excellent precision. Hadrons, which experience strong interaction, deposit their energy mostly in the hadron calorimeter(HCAL) which is the next layer of ECAL. The superconducting solenoid is located between the HCAL and the muon chambers. The muon chambers are employed to determine the trajectory of muons in combination with the tracking sub-detector. Neutrinos barely interact with matter, anal-

ysis techniques are required for the reconstruction of neutrinos. Figure 3.3 demonstrates how various elementary particles interact with the layers of sub-detectors in the CMS.

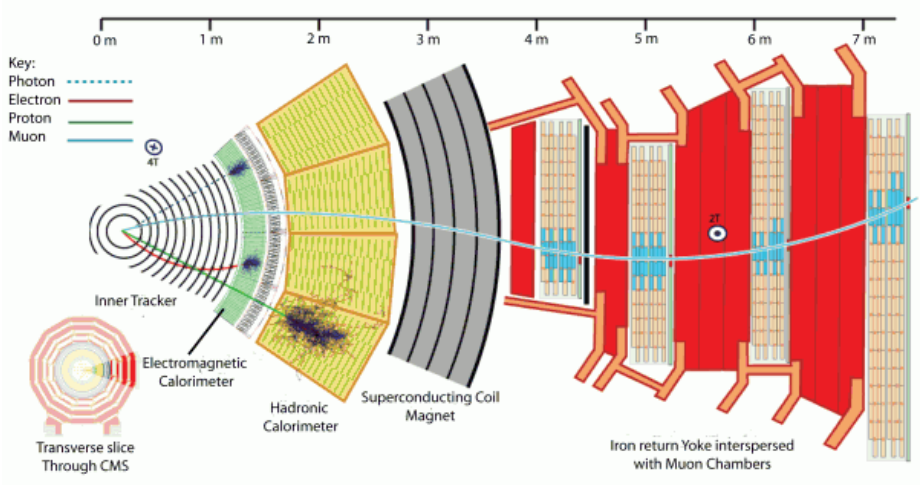

Figure 2.3: Transverse view of a slice of the CMS detector. A muon, manifested by a blue line, curves through the magnetic field and leaves hits in the tracking sub-detector. The muon also makes hits in the muon chamber and curves in opposite direction. An electron, represented by a red line, bends through the magnetic field, leaves hits in the inner tracker, and deposits its energy in the ECAL. The dashed blue line illustrates a photon, and it deposits most of the energy in the ECAL sub-detector. The green lines represents hadrons and they deposit most of their energy in the HCAL.

2.2.1 Coordinate Convention

A cylindrical coordinate system is commonly used, with the azimuthal angle phi. The polar angle theta is measured from the z-axis and the pseudo rapidity is defined as η = -ln $tan(\theta/2)$.

2.2.2 Superconducting Solenoid

The superconducting solenoid in the CMS provides a magnetic field of 3.8 T. When a charged particle with momentum enters a magnetic field, the trajectory of the charged particle is governed by Lorentz force, i.e. a charged particle of mass m moving with velocity v under a perpendicular magnetic field B will follow a circular path with a bending radius of rho = p/qB, where p = mv, where the charge is q.

2.2.3 Tracking Detectors

Charged particles remains paths by leaving their positions as they transverse the sensors of the CMS tracker. These paths helps to reconstruct high-energy electrons, muons, hadrons, and products of b-quark decay. As charged particles travel through the sensors, they ionise the silicon by liberating electrons. Those electrons are guided by an electric field so that they can be collected by a read-out. The CMS tracking detectors consists of a silicon pixel sub-detector and a silicon microstrip sub-detector. The silicon pixel sub-detector is located closest to the interaction point and the silicon microstrip sub-detector surrounds the pixel sub-detector.

2.2.4 Caloriemeter Subdetectors

The CMS detector two layers of scintillating calorimeters, the electromagnetic calorimeter and the hadron calorimeter. Those calorimeters are meant to deposit most of the energy from collisions. The calorimeters generally consist of absorbing layers and active layers side by side. The active layers of scintil-

lating medium produces photons as incident radiation excites the atoms. The electromagnetic calorimeter mostly deposits energies of electrons and photons and makes electromagnetic showers, the hadron calorimeter mostly absorbs energies of hadrons.

2.2.5 Muon Detectors

CMS has three types of gaseous particle detectors for muon identification. In the barrel region, four layers of drift tube (DT) chambers are used. In the end-cap regions, cathode strip chambers(CSC) are used. Resistive plate chambers (RPCs) are located in both the barrel and the end-cap regions. The RPCs produce a fast response, but poorer position resolution than DTs and CSCs. In muon system, there are about 1400 muon chambers total, 250 DTs, 540 CSCs, and 610 RPCs.

2.2.6 Trigger

The trigger selects the physics event by checking if an event is suitable for a physics analysis. The LHC makes about 10^9 interactions per second at designed luminosity when the bunch crossing rate is 40 MHz, while data from only about 10^2 crossings per second can be written with the limited storage. Thus, the trigger system has to accomplish a rejection factor of nearly 10^6. There are two steps in the CMS trigger system; Level-1(L1) trigger and High-Level Trigger(HLT).

The Level-1(L1) trigger selects events by using a small amount of key information such as features of high energy jets, muons, missing transverse energy,

within around 1s. field-programmable gate arrays(FPGA) enables these fast calculations. After this L̈evel-1c̈alculation, the event rate becomes around 50 kHz which is about thousand down from all the data. If an event passes Level 1 trigger, all the data in the buffer of the detector is transferred to H́igh Levelt́rigger. As the event rate at the High Level trigger is reduced to 50 kHz by Level-1 trigger, the High Level trigger can analyse the events with much more time than the Level-1 trigger. The High Level trigger cut down the event rate to 1000 events per second and those remaining events are stored on tape for analysis.

Chapter 3

Data and Simulated Sample

This chapter introduces the Monte Carlo samples of the charged Higgs signal events and the SM background processes. The SM ttbar semi-leptonic channel is the major irreducible background of this analysis. One of other important backgrounds is W+jets process with four or more jets, when the W decays to one lepton and a neutrino. Single top quark + jets becomes another important background when $t \to Wb \to l\nu b$. Other backgrounds contains Z+jets with Z decaying to two leptons and only one lepton is detected as a prompt lepton. Diboson+jets (WW, WZ, ZZ) sample with non-prompt lepton decays from those bosons are taken into account. These SM processes are simulated with CMS detector as described in Sec.3.1. Data stream used in this analysis with single lepton triggers are pronounced in Sec.3.2. QCD multijet background events having a fake lepton from jets are driven from data which is described in detail later in Sec.4.1.2.

3.1 Simulation Samples

Signal samples are generated privately following the CMS central MC production procedures. PYTHIA 6.4.26 [31] is used to generate and hadronize the signal $t\bar{t}$ events; t decyas to $H^{\pm}$ and a b quark and $\bar{t}$ to W^{-} and $\bar{b}$. Then the charged Higgs decays to $c\bar{b}$, and the W^{-} decays to an electron or a muon and accompanying neutrino in all the times. The signal $t\bar{t}$ samples are prepared for the $H^{\pm}$ masses of 90, 100, 110, 120, 130, 140, and 150 GeV/c^2.

Background samples of the SM processes are listed in the Tab. 3.1. Mainly MADGRAPH 5.1.3.30 [22] is used for the event generation of the Monte Carlo samples except for the single top and di-boson samples for which POWHEG v1.0 r1380 [25] and PYTHIA are used respectively. PYTHIA is interfaced for the parton showering. Corresponding effective luminosity for each simulation sample is listed in the Tab. 3.1. Systematic samples for the $t\bar{t}$ events are listed in Tab. 3.2. Uncertainties from the event generator selection is estimated by comparing the $t\bar{t}$ generated with POWHEG v1.0 (NLO) to the MADGRAPH (LO) sample in Tab. 3.1.

3.2 Data samples and Trigger

The CMS data at $\sqrt{s} = 8\ TeV$, with total integrated luminosity 19.7 fb^{-1}, is used for this analysis. For the muon + jets channel, events are accumulated in a SingleMu stream and triggered by HLT_IsoMu24_eta2p1_v* which requires an isolated single muon trigger with a pT threshold of 24 GeV/c and $|\eta|$ threshold of 2.1. For the electron + jets channel, the HLT path is HLT_Ele27_WP80_v*

Table 3.1: List of simulation samples of SM background processes

Process	Dataset	Eff. lum. (pb^{-1})
$t\bar{t}$	TTJets_MSDecays_central_TuneZ2star_8TeV-madgraph-tauola/	214.9k
SingleTop	Tbar_s-channel_TuneZ2star_8TeV-powheg-tauola/	79.53k
	Tbar_t-channel_TuneZ2star_8TeV-powheg-tauola/	50.13k
	Tbar_tW-channel-DR_TuneZ2star_8TeV-powheg-tauola/	44.45k
	T_s-channel_TuneZ2star_8TeV-powheg-tauola/	68.59k
	T_t-channel_TuneZ2star_8TeV-powheg-tauola/	65.89k
	T_tW-channel-DR_TuneZ2star_8TeV-powheg-tauola/	44.83k
W+jets	WJetsToLNu_TuneZ2Star_8TeV-madgraph-tarball/	1531.9
DY+jets	DYJetsToLL_M-10To50_TuneZ2Star_8TeV-madgraph/	3418.5
	DYJetsToLL_M-50_TuneZ2Star_8TeV-madgraph-tarball/	8625.0
VV	WZ_TuneZ2star_8TeV_pythia6_tauola/	289.4k
	ZZ_TuneZ2star_8TeV_pythia6_tauola/	555.1k
	WW_TuneZ2star_8TeV_pythia6_tauola/	174.7k
ttV	TTWJets_8TeV-madgraph/	289.4k
	TTZJets_8TeV-madgraph_v2/	555.1k
	TTH_Inclusive_M-125_8TeV_pythia6/	174.7k

for the events in SingleElectron stream. Selected electron events are required to have a single isolated electron with a pT greater than 27 GeV/c and $|\eta|$ smaller than 2.5. Those datasets withp corresponding luminosities are listed in Tab. 3.3.

Table 3.2: List of simulation samples of $t\bar{t}$ systematic uncertainties. Effective luminosities are calculated using the $\sigma_{t\bar{t}} = 252.89$ pb.

Process	Dataset	Eff. lum. (pb^{-1})
Various Top Qurak Mass		
M(t) = 171.5	TTJets_MSDecays_mass171_5_TuneZ2star_8TeV-madgraph-tauola/	75.1k
M(t) = 173.5	TTJets_MSDecays_mass173_5_TuneZ2star_8TeV-madgraph-tauola/	100.3k
Event Generator and Parton Showering		
POWHEG & PYTHIA	TT_CT10_TuneZ2star_8TeV-powheg-tauola/	83.8k
Q^2 Scale		
Scale up ($\times$ 4)	TTJets_MSDecays_scaleup_TuneZ2star_8TeV-magraph-tauola/	123.4k
Scale down ($\times$ 0.25)	TTJets_MSDecays_scaledown_TuneZ2star_8TeV-magraph-tauola/	153.2k
Matching up ($\times$ 4)	TTJets_MSDecays_matchingup_TuneZ2star_8TeV-magraph-tauola/	116.2k
Matching down ($\times$ 0.25)	TTJets_MSDecays_matchingdown_TuneZ2star_8TeV-magraph-tauola/	81.5k

Table 3.3: List of CMS datasets for pp collisions at $\sqrt{s} = 8$ TeV

Data set	Luminosity (fb^{-1})
SingleMu/Run2012A-22Jan2013-v1/AOD	0.886
SingleMu/Run2012A-22Jan2013-v1/AOD	4.435
SingleMu/Run2012A-22Jan2013-v1/AOD	7.125
SingleMu/Run2012A-22Jan2013-v1/AOD	7.246
SingleElectron/Run2012A-22Jan2013-v1/AOD	0.876
SingleElectron/Run2012A-22Jan2013-v1/AOD	4.420
SingleElectron/Run2012A-22Jan2013-v1/AOD	7.132
SingleElectron/Run2012A-22Jan2013-v1/AOD	7.294

Chapter 4

Event Selection

The charged Higgs boson in $t\bar{t}$ signal event contains one prompt lepton, one neutrino, and four quarks; $t\bar{t} \to b(H^{\pm})\bar{b}W \to b\bar{b}(c\bar{b})l\nu_l$. Thereby, we expect to have the final state objects, a muon or an electron, at least four reconstructed jets, and missing transverse energy from the balance of p_T sum of the all observed final state objects. This section describes the identification of each final state object and the $t\bar{t}$ event selection criteria.

4.1 Object Identification and Selection

Final state objects used in this analysis are reconstructed using the standard CMS particle-flow (PF) algorithm [4]. This algorithm reconstruct five types of objects -muon, electron, photons, neutral hadrons, and charged hadrons- coherently exploiting all the CMS sub-detector. It also reconstructs vertices using associated tracks. Among them, a vertex with highest $\sum p_T^2$ is marked as the primary vertex. An additional set of identification criteria are applied to the objects in order to use in the analysis.

A set of quality cuts is applied to the muon selection [6]. At first the muon is set to be a global muon which has the inner detector track matched to at least two muon stations. The track fit has a $\chi^2/ndof < 10$ and leaves hits more than five track layers. There should exist nonzero number of valid hits and at least one pixel hit. The muon track is required to have 2D impact parameter w.r.t the primary vertex less than 0.2 cm and the z distance w.r.t the primary vertex less than 0.5 cm. In order to use the muon in the analysis, a tight muon selection is required as having $p_T > 26GeV/c$, $|\eta| < 2.1$, and the relative isolation (Iso_{rel})[1] to be less than 0.12. The $\mathrm{Iso_{rel}}$ is calculated by summing all the energies within a cone of $\Delta R < 0.4$ around the selected muon track divided by the muon p_T.

Electrons are reconstructed and identified based on the EGamma recommendation [5]. Electrons directing to the barrel-endcap transition gap ($1.4442 < |\eta_{sc}| < 1.5660$) are excluded. Conversion photon is vetoed and the tt mva-TrigV0 ID is to be larger than 0.9. The 2D impact parameter with respect to the primary vertex is required to be less than 0.02 cm. The Iso_{rel} is calculated in a same way with the muon but using $\Delta R < 0.3$ cone with the effective area correction that is applied to the neutral pileup energy. A Iso_{rel}[2] cut is imposed on 0.1. Additionally, the electron p_T is required to have at least 30 GeV/c within $|\eta| < 2.5$.

Jets are clustered using all the particle flow candidates except an isolated leptons and pile up candidates. The anti-kt algorithm [24] with a distance

[1] $Iso_{rel}(\mathrm{muon}) = (\sum \mathrm{p_T^{CH}} + \max(0.0, \sum \mathrm{p_T^{NH}} + \sum \mathrm{p_T^{PH}} - 0.5 * \sum \mathrm{p_T^{PU,CH}}))/\mathrm{p_T}(\mu)$

[2] Iso_{rel} (electron) $= (\sum \mathrm{p_T^{CH}} + \max(0.0, \sum \mathrm{p_T^{NH}} + \sum \mathrm{p_T^{PH}} - \rho * \mathrm{A}))/\mathrm{p_T}(electron)$, where ρ is the pileup energy density and A is the effective area defined by electron pseudorapidity.

parameter (ΔR) of 0.5 is used. A series of corrections [7] are applied to the jet energy that covers pileup offset, simulated response, and residual η and p_T dependences for data. The jet resolution is smeared additionally in the simulation sample. Using up to the L3 correction, the PF jet with loose ID has an efficiency of greater than 99%, with no need to apply addition SFs. More quality cuts are applied to the selected PF jets as listed below.

- Jet identifies not coming from PU with loose WP
- Neutral Hadron Energy Fraction < 0.99
- Neutral EM Energy Fraction < 0.99
- More than 1 constituents construct a jet
- Charged hadron energy fraction > 0
- Charged multiplicity >0
- Charged em energy fraction < 0.99
- Muon energy fraction < 0.8
- $p_T > 30$ GeV/c, $|\eta| < 2.4$

Missing transverse momentum (MET) is defined as the negative vector sum of the momenta of all reconstructed particles in the orthogonal direction of the beam [15]. Pile up correction (Type-0), a propagation of the jet energy corrections (Type-1), and the ϕ corrections (xy-shift) are applied to the PF MET (PFMET).

4.1.1 Pre-selection cuts

The $t\bar{t}$ events in the lepton+jets channel are selected requiring one lepton passing a tight selection criteria, at least four jets, and corrected missing transverse energy. No other e (or μ) with $p_T > 20(10)$ GeV/c within $|\eta| < 2.5$, relative isolation less than 0.3(0.3), and TrigMVA > 0.5 (isGlobal) is allowed except the initial tight lepton. The pile up event reweight is done in the simulation event, to ensure the number of vertices in the simulation matches that in the data. Trigger, lepton ID and isolation scale factors are applied to the MC events following the Top Reference Selection for run1 recommendation. Since the signal $t\bar{t}$ event includes one neutrino in the final state, PFMET greater than 20 GeV/c is applied. The number of vertices and number of jets in the simulation samples shows a good agreement between the MC samples and the data after the selection in Fig. 4.1. The discrepancy in the high jet multiplity bins is a known priori in the $t\bar{t}$ event selection. We would not apply additional corrections for that because the kinematic distribution which is important to this analysis does agree each other.

The signal $t\bar{t}$ event includes three b quarks in the final state while the SM $t\bar{t}$ event has two. We use the Combined Secondary Vertex tagging with medium working point (CSV>0.679) [17] to tag the b jets. Fig. 4.2 compares the number of CSVM tagged jets in the SM $t\bar{t}$ events with that in the $H^{\pm}$ signal $t\bar{t}$ events. The events with two or more b-tagged jets are taken as a signal region in this analysis, and the event with only one b-tagged jet is used as a control sample where the QCD contribution is estimated.

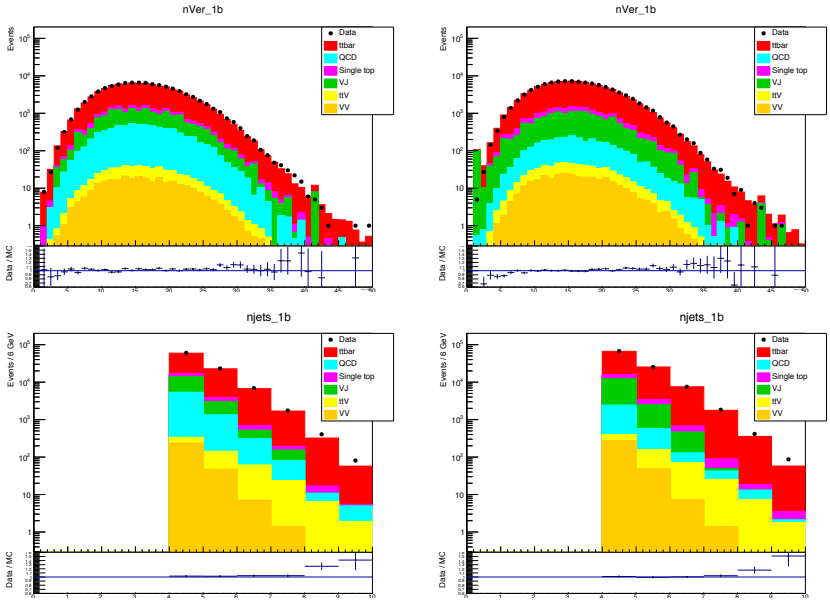

Figure 4.1: Plots in 1 b-tag region. Upper left plot: number of vertices for e+jets channel, upper right plot: number of vertices for μ+jets channel, bottom left plot: jet multiplicity for e+jets channel, bottom right plot: jet multiplicity for μ+jets channel.

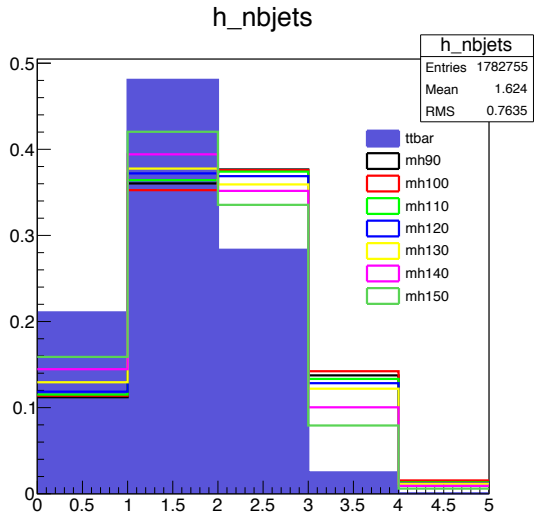

Figure 4.2: Normalized number of b-jets in the SM $t\bar{t}$ sample (light blue filled) compared with the $H^{\pm}$ signal $t\bar{t}$ sample (colored lines).

4.1.2 Data driven QCD sample

The QCD contribution is driven from the single electron/muon data in the control (one b-tagged) region. This approach on QCD multi-jet events is previously used by charged Higgs to $c\bar{s}$ analysis [19]. The basic idea is that the QCD multijet events in the signal selection region is derived from the lepton anti-isolated region. The normalization[3] of the QCD event from the anti-Iso_{rel} is calculated by the ratio of QCD events in the isolated region ($Iso_{rel} < 0.1(e)/0.12(\mu)$) to the anti-isolated region ($0.1(e)/0.12(\mu) < Iso_{rel} < 0.3$) in the low MET area ($< 20$ GeV/c) where the QCD events are thought to be rich. Fig. 4.3 demonstrates the Iso_{rel} distribution with MET < 20 GeV/c for e/μ+jets events in data and other MC backgrounds samples. It is assumed that the discrepancy between the data and the simulated SM processes in the Iso_{rel} distribution is the QCD multi-jet events. Obtained scale factors are shown in the Tab. 4.1 in six exclusive lepton η regions to account the QCD events in the forward region. QCD kinematic distribution is obtained by QCD SF weight applied to the QCD distribution which is derived in the anti-isolated region with MET > 20 GeV/c for each lepton η. Total QCD yields are estimated by adding those QCD events on top of each other over the entire η regions.

[3] Scale Factor $= \frac{(\text{Data}-\text{Other bkgds})_{\text{iso}}}{(\text{Data}-\text{Other bkgds})_{\text{anti}-\text{iso}}}$

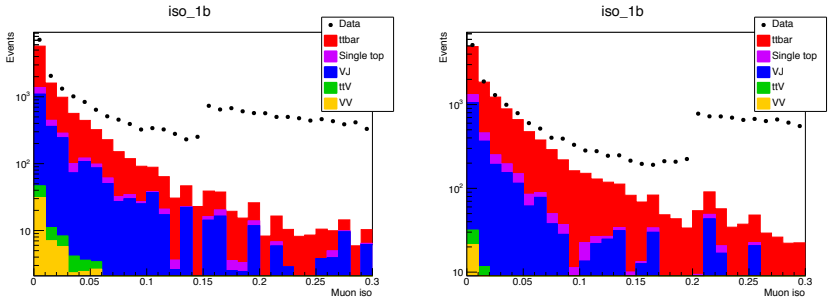

Figure 4.3: Lepton relative isolation in 1b-tagging region

Table 4.1: QCD scale factors for e+jets and μ+jets channel

$\eta(e)$	(-2.5,-2.0)	(-2.0,-1.5)	(-1.5,0)	(0,1.5)	(1.5,2.0)	(2.0,2.5)
Control Region (1b-tag)	1.247	0.793	0.411	0.368	0.757	1.141
Signal Region (2b-tags)	1.334	0.732	0.283	0.318	0.489	1.627
$\eta(\mu)$	(-2.1,-1.8)	(-1.8,-1.5)	(-1.5,0)	(0,1.5)	(1.5,1.8)	(1.8,2.1)
Control Region (1b-tag)	0.406	0.304	0.168	0.181	0.327	0.386
Signal Region (2b-tags)	0.437	0.356	0.129	0.143	0.419	0.132

4.2 Treatment on two or more b-tagged Sample

In this analysis signal region is requiring two b-tagged jets and more than two b-tagged jets separately. Top quark background events have relatively large statistics, however non-top-quark (non-t) background is suffered from the small statistics in the multi b-tagged selection. Since we perform a shape analysis for the search, having smooth shape is very important. For this reason, special treatment has applied to those non-top backgrounds.

Events in VV and V+jets events are selected by requiring CSVM up to two b-tagged jets. Then, the yield in the 3 b-tagged region is estimated by

applying the mis-tag rate to the un-tagged jets in the 2 b-jets events. With the application of both b-tagging for two jets and mis-tag rate to the un-tagged jets, the shape of the di-jet mass distribution for non-t background events is improved.

4.3 Event Yields and Control Region Plots

In order to understand and test the simulated samples with the data, the 1 b-tagged events are used for the control sample. The QCD scale factors are obtained in the 1 b-tagged region and 2 b-tagged region separately. The QCD scale factors obtained in the 1 b-tagged region is applied to the QCD estimation in 1 b-taggged region, and the QCD scale factors from 2 b-tagged region are applied to the QCD estimation in 2, 3 b-tagged selection. The event yields are listed in Tab. 4.2 and Tab. 4.3 for the e+jets and μ+jets selection, respectively.

Table 4.2: Event yields with the e+jets selection from MC samples and data corresponding to 19.7 fb^{-1} at $\sqrt{s} = 8$ TeV

e+jets	1b-tag	2b-tag	3b-tag
ttbar	69288.7	43591.5	4006.5
QCD	6473.9	1238.2	106.5
Single Top	4068.77	1881.5	147.3
W/Z+jets	10351	1097.9	79.1
$WW/WZ/ZZ$	289.9	55.5	5.4
tt+$W//H$	279	168.5	34.7
Total Bkgd	90751.3	48033.4	4379.5
Observed	92877	50542	4848

Table 4.3: Event yields with the μ+jets selection from MC samples and data corresponding to 19.7 fb^{-1} at $\sqrt{s} = 8$ TeV

μ+jets	1 b-tag	2 b-tag	3 b-tag
ttbar	81622.4	51823.2	4655.05
QCD	2500.33	614.945	59.0368
Single Top	4828.79	2211.66	169.064
W/Z+jets	11981.9	1305.49	64.4039
$WW/WZ/ZZ$	322.197	195.441	6.86
tt+$W/Z/H$	322.197	195.441	40.515
Total Bkgd	101585.43	56212.79	5094.93
Observed	102424	57593	5754

Fig. 4.4 show the number of jets and MET of the e/μ+jets in the control region. The p_T and η distributions of the lepton and four leading jets in the control region are compared in the Fig. 4.5 and Fig. 4.6. This comparison shows that the simulation samples especially in the kinematic distribution have quite a good agreement with the data.

Data to MC agreement in 2 b-tags signal region is seen in Fig. 4.7 and 4.8, and 3 b-tag signal region observable kinematic distributions are compared in Fig. 4.9 and 4.10 for e+jets and μ+jets selection together.

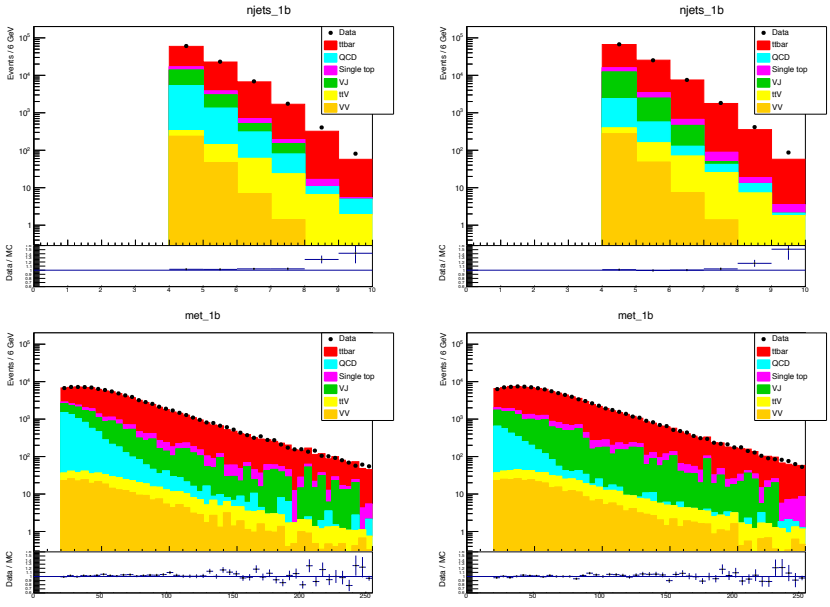

Figure 4.4: Plots in 1b-tagging region. Upper left plot: jet multiplicity for e+jets channel, upper right plot: jet multiplicity for μ+jets channel, bottom left plot: MET for e+jets channel, bottom right plot: MET for μ+jets channel

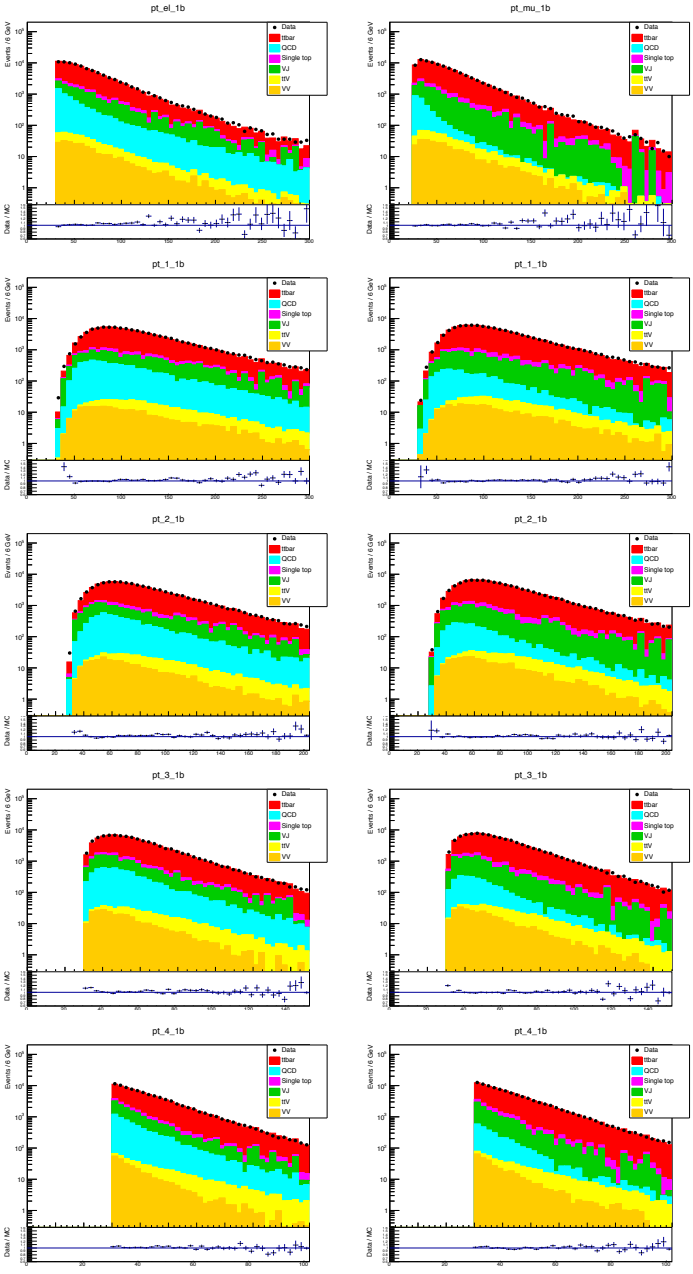

Figure 4.5: Control region: p_T distributions of e(left)/μ(right) and four jets in order.

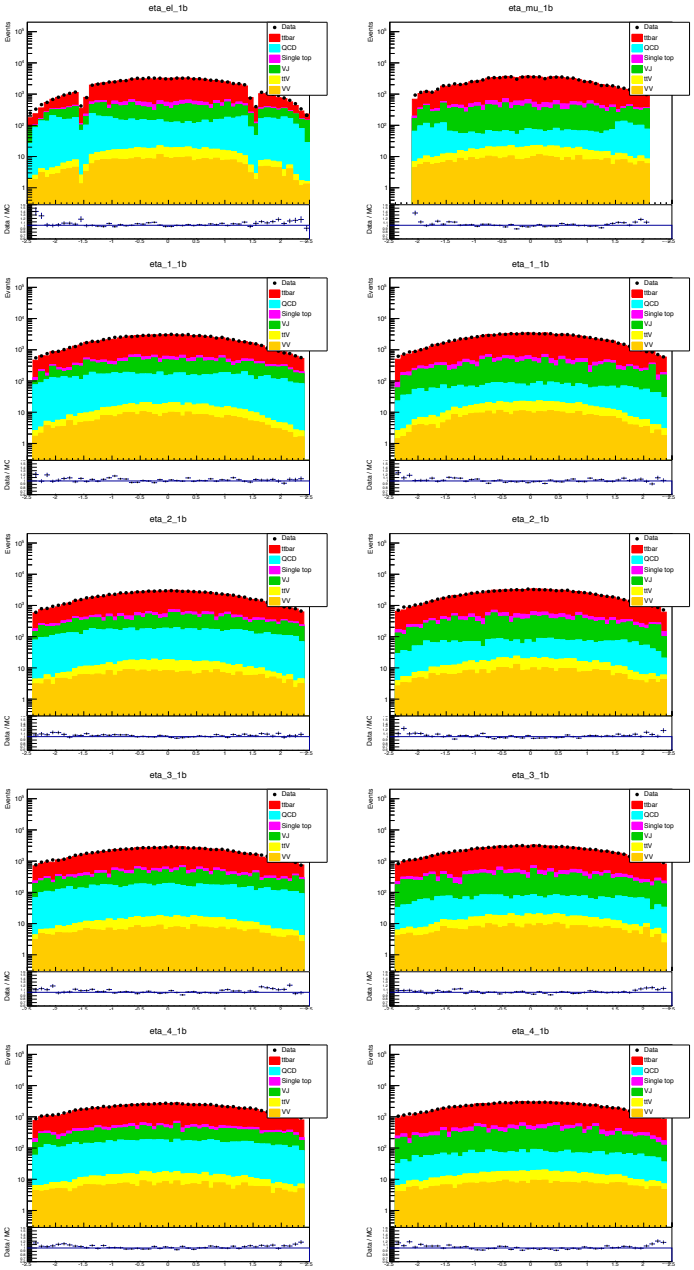

Figure 4.6: Control region: η distributions of e(left)/μ(right) and four jets in order.

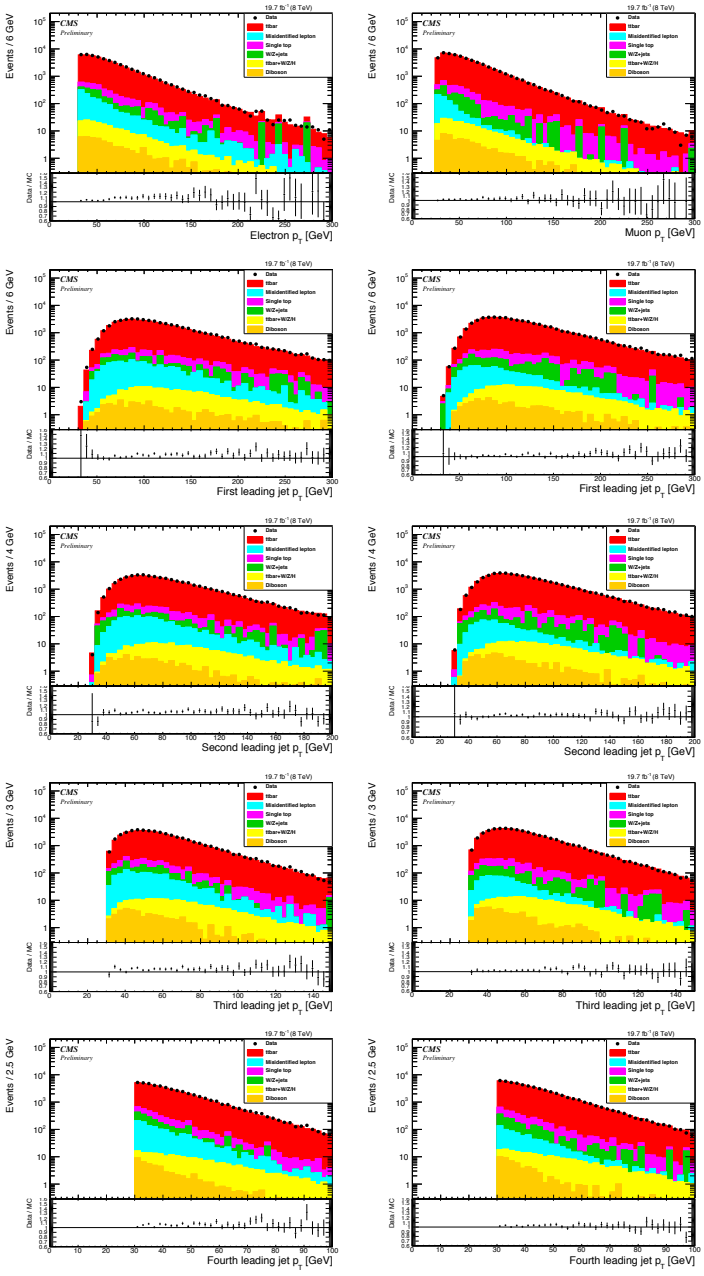

Figure 4.7: Signal Region: p_T distributions of lepton+4jets in 2 b-tags region.

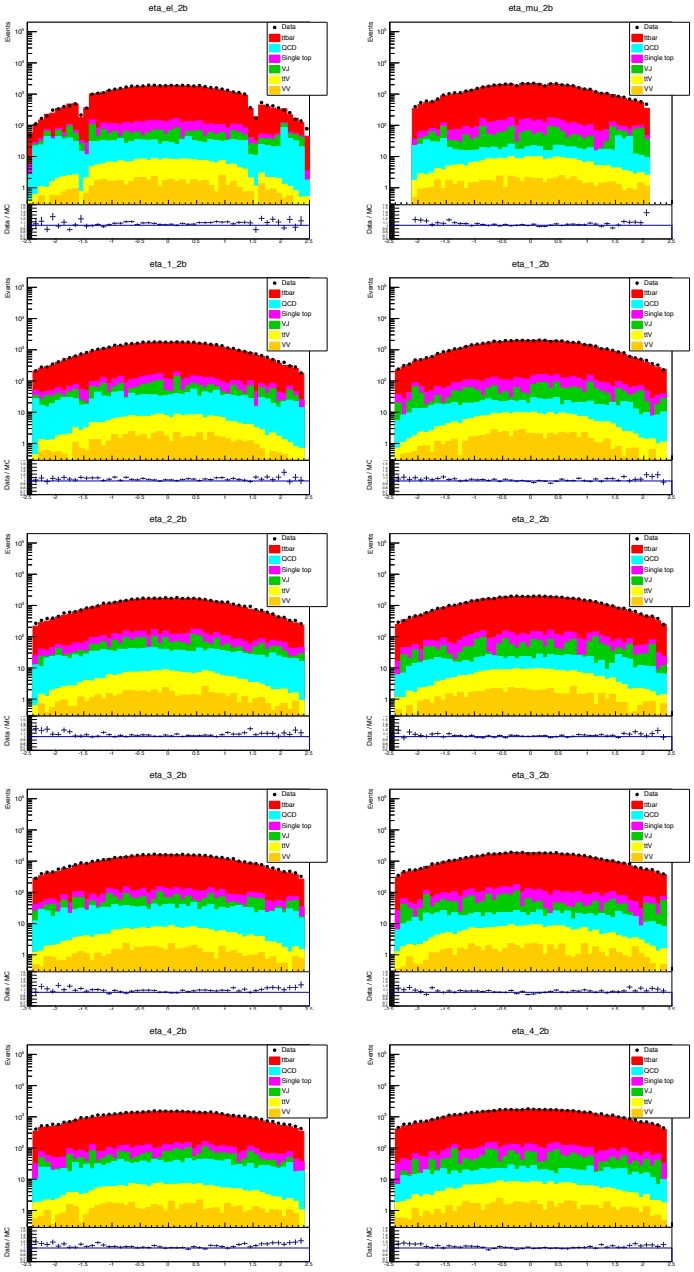

Figure 4.8: Signal Region: η distributions of lepton+4jets in 2 b-tags region.

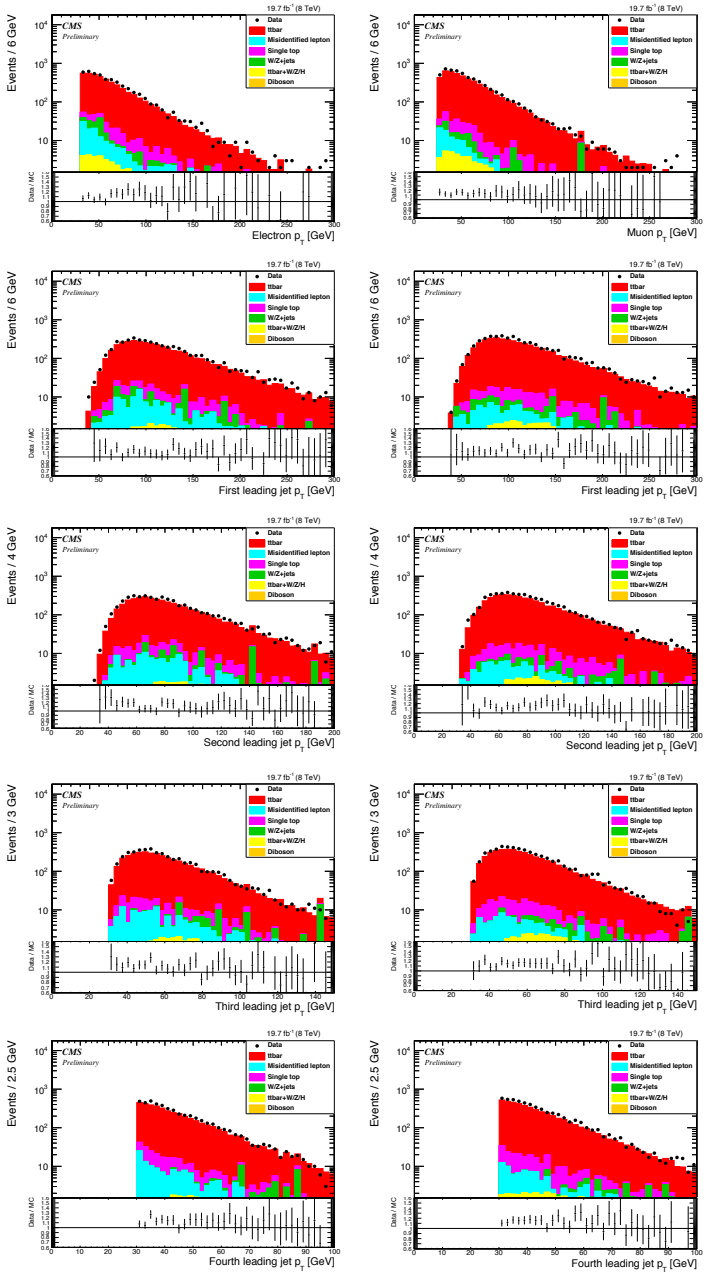

Figure 4.9: Signal Region: p_T distributions of lepton+4jets in 3 b-tags region.

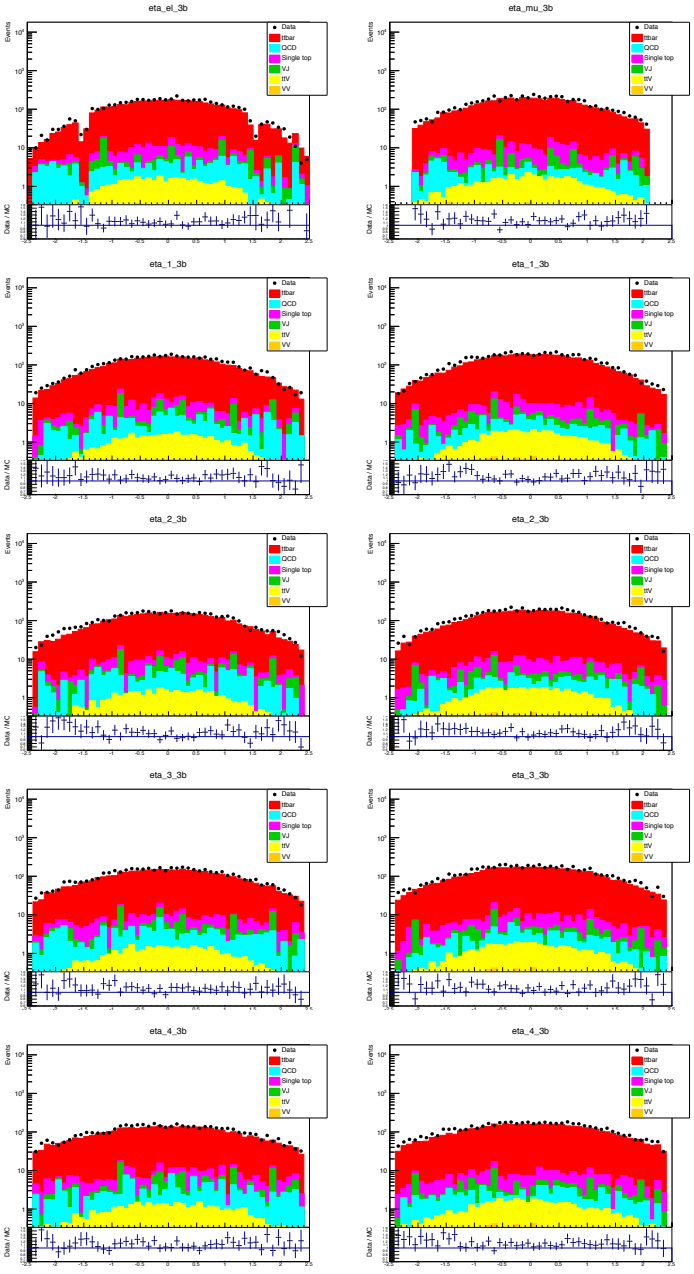

Figure 4.10: Signal Region: η distributions of lepton+4jets in 3 b-tags region.

Chapter 5

Top Specific Correction

In order to search for a secondary peak over SM di-jet invariant mass, having a good mass resolution is very important. In addition to the generic jet energy corrections that give a correction up to detector level, jet pT correction up to parton level is necessary to full reconstruction of the top quark events in both data and simulation samples. Thus, the jet energy response function f is defined in Eq. 5.1 comparing the parton p_T and the reconstructed jet p_T.

$$f = \frac{p_T(parton) - p_T(jet)}{p_T(jet)} \tag{5.1}$$

The response function is used for a reconstructed jet to compensate the loss from the generated parton energy, as referred to a top specific (TS) correction. Among the four partons generated in the lepton+jets channel SM $t\bar{t}$ events, two of them are decay products of W and other two are b and $\bar{b}$ quarks from t and $\bar{t}$, respectively. The matching between parton and reconstructed jet is done based on the physics definition, within $\Delta R < 0.3$. When more than one jet is matched to a sample parton, the events are discarded. Only the events

with four partons matched to each jet are used in this jet response study.

The jet response is fitted as a function of p_T in Eq. 5.2 by fitting parameters separately by its parton flavour(b, c, and $u/d/s$/g) as seen in Fig. 5.1. This response function fit is repeated for nine different jet η region: ($|\eta|$: 0, 0.174, 0.348, 0.522, 0.696, 0.879, 1.131, 1.392, 1.74, 2.5). For the p_T response of a jet matched to a b-quark, $|\Delta p_T| < 25$ GeV/c is applied to prevent over-correction. Then, the p_T response is fitted to the fitting function,

$$f(p_T) = a + b \times \sqrt{p_T} + \frac{c}{p_T} + d \times p_T. \tag{5.2}$$

With the TS correction, corrected jet p_T should have closer to the corresponding parton p_T. Thereby, the jet p_T response (f) using corrected jet p_T is calculated again as a 1-D distribution in selected p_T and η bin: (p_T: 30, 40, 50, 60, 70, 80, 90, 100, 120, 150, 300) and the same η bin as above. The response distributions are shown for the case of the $|\eta| < 0.174$ in Fig. 5.2 and for various η with 100 GeV/c $< p_T <$ 120 GeV/c in Fig. 5.3. Uncertainty of the TS correction is obtained from the width of Gaussian fit of the distribution. The widths in each $|\eta|$ region are again fitted to a function of p_T (Eq. 5.2) as shown in Fig. 5.4.

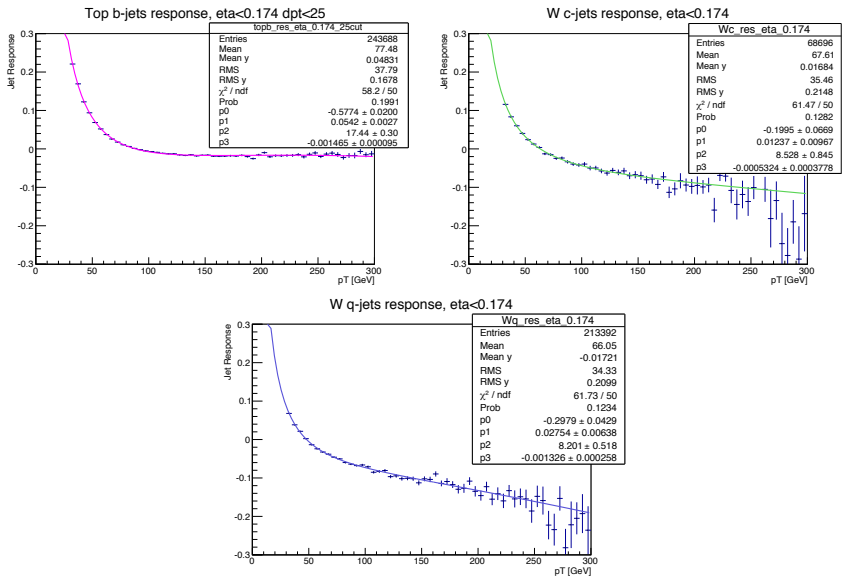

Figure 5.1: Jet p_T responses as a function of reconstructed p_T for a b-quark jet, c-quark jet, and light-flavour jet where $|\eta|$ is smaller than 0.174

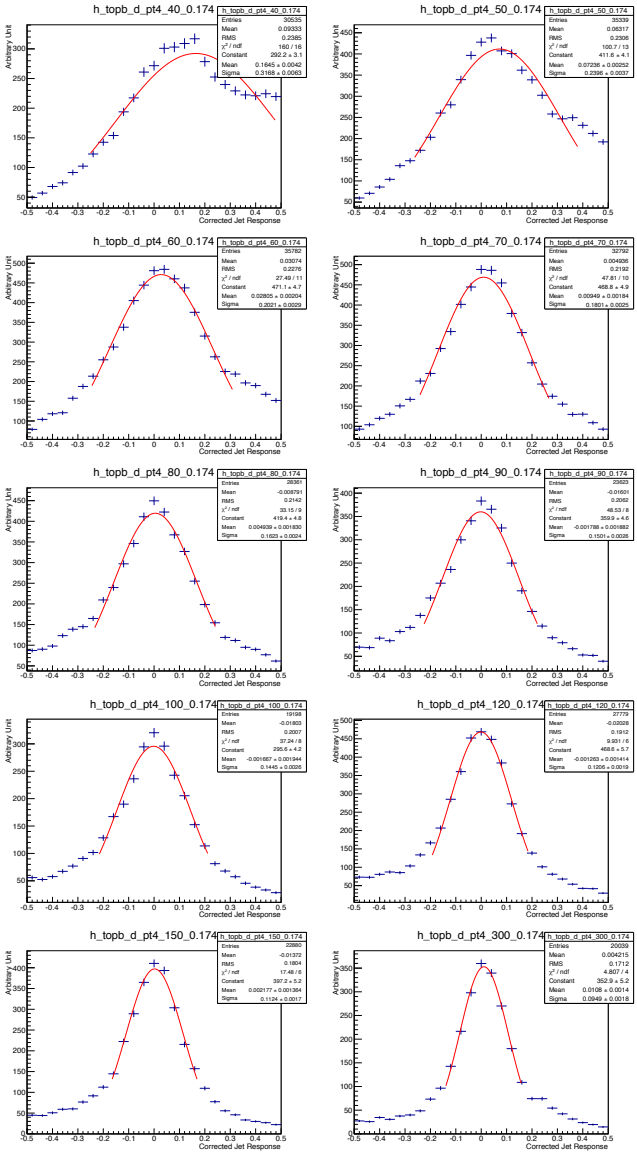

Figure 5.2: Corrected p_T response distributions for b-quark jet where $|\eta|$ is smaller than 0.174. From the top left, p_T ranges (30,40), (40,50), (50,60), (60,70), (70,80), (80,90), (90,100), (100,120), (120,150), and (150,300).

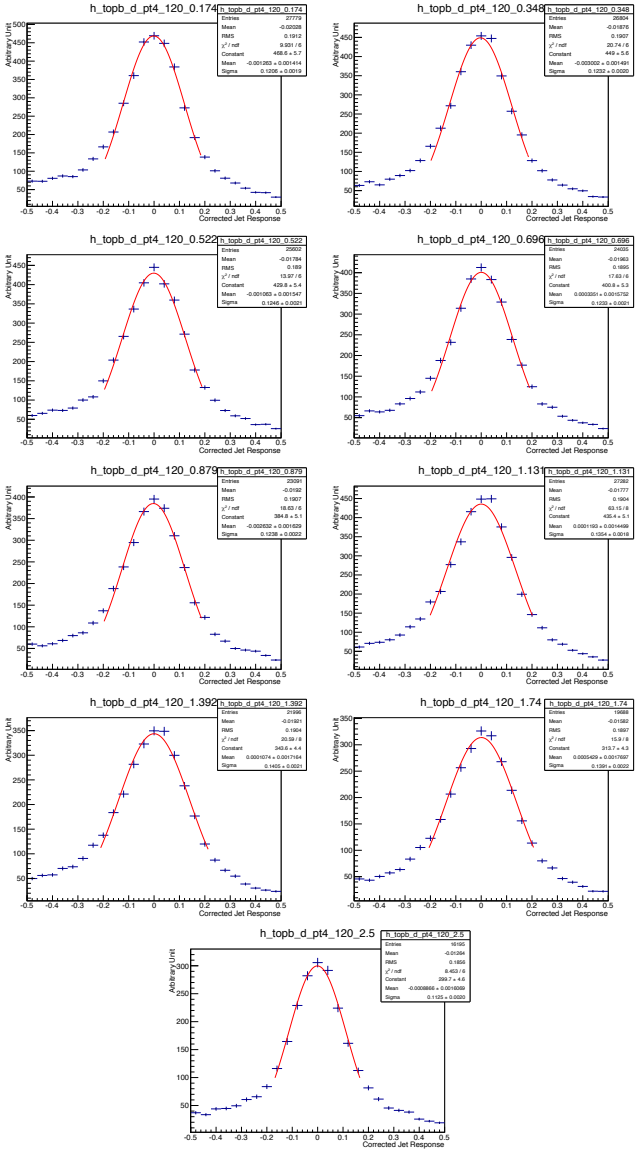

Figure 5.3: Corrected p_T response distributions for b-quark jet where jet pT is between 100 GeV/c^2 to 120 GeV/c^2. From the top left, η ranges are (0,0.174), (0.174,0.348), (0.348,0.522), (0.522,0.696), (0.696,0.879), (0.879,1.131), (1.131,1.392), (1.392,1.740), and (1.740,2.5).

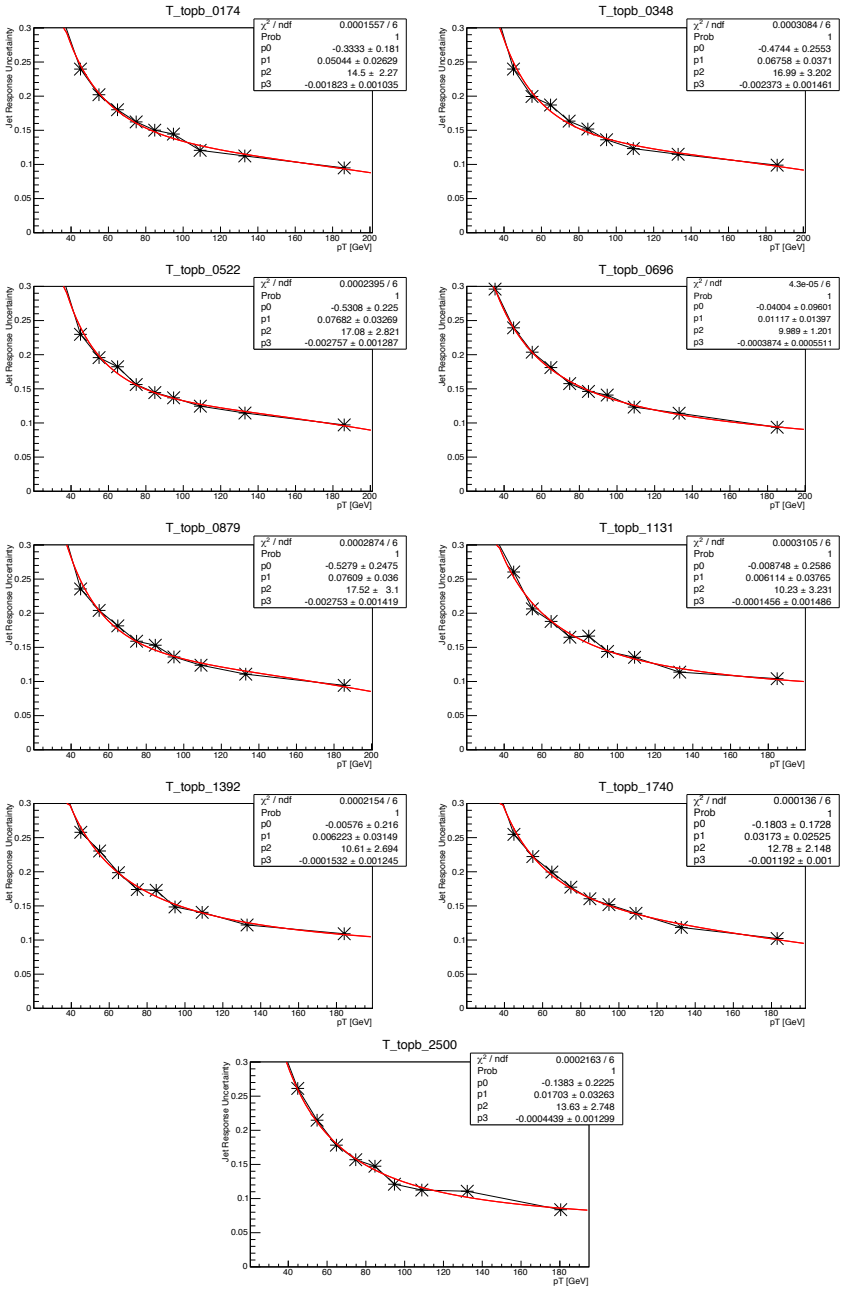

Figure 5.4: Parametric fit of the TS correction uncertainty of b-quark jet as a function of p_T in nine different η region

5.1 Top Specific Correction Performance

The di-jet invariant mass distribution before and after the TS correction is compared in the Fig. 5.5. Those two jets are from the W in the SM $t\bar{t}$ events, and from the $H^{\pm}$ in the signal $t\bar{t}$ samples. With the TS correction the mean value of the di-jet mass distribution is closer to the true value, and its resolution is improved by 7∼9 % in both samples. The test is also done for the hadronic side top quark mass, M($bq\bar{q}$) and M($bc\bar{b}$, in Fig. 5.6. The improvement is observed as well.

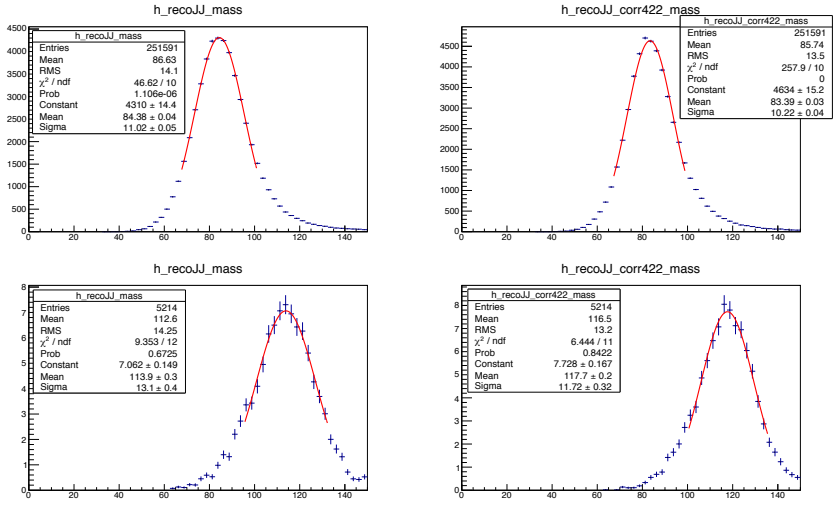

Figure 5.5: Top plots show M(jj) in the SM $t\bar{t}$ before (left) and after (right) the TS correction and bottom plots are M($c\bar{b}$) of 120 GeV/c^2 $H^{\pm}$ sample before (left) and after (right) the TS correction.

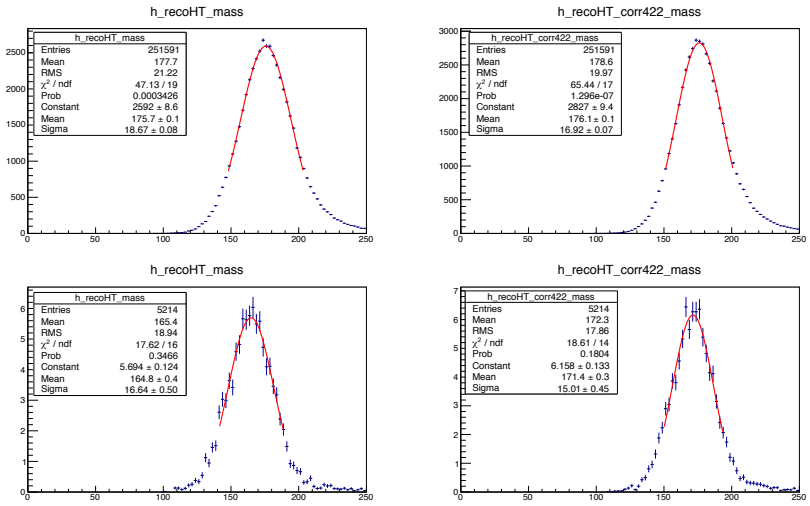

Figure 5.6: Top plots are the SM hadronic side top quark mass, M(bjj), before (left) and after (right) the TS correction. Bottom plots are M($bc\bar{b}$) of 120 GeV/c^2 $H^{\pm}$ $t\bar{t}$ sample before (left) and after (right) the TS correction.

Chapter 6

$t\bar{t}$ Event Reconstruction

6.1 Kinematic fitter

A kinematic fit of the $t\bar{t}$ is performed to find the right assignment of four jets to the each partons in the semi-leptonic decays of $t\bar{t}$ and to improve the resolution of di-jet invariant mass. In the selected events, only four leading jets are assumed to be from the tree level partons and used for the $t\bar{t}$ reconstruction. TS correction is applied to those selected jets in the kinematic fitter by its assigning parton flavor. For example, one jet is assigned to a place of b-quark of the $t\bar{t}$, the input p_T of the jet is having the TS correction for the b flavour applied automatically. Uncertainty of the TS correction is used to the denominator of the χ^2 term in the Eq. 6.1. The χ^2 is defined as

$$\begin{aligned}\chi^2 = & \sum_{i=l,4jets} \frac{(p_T^{i,fit} - p_T^{i,meas})^2}{{\sigma_i}^2} + \sum_{j=x,y} \frac{({p_j}^{UE,fit} - {p_j}^{UE,meas})^2}{{\sigma_{UE}}^2} \\ + & \frac{(M_{l\nu} - M_W)^2}{{\Gamma_W}^2} + \frac{(M_{bl\nu} - M_t)^2}{{\Gamma_t}^2} + \frac{(M_{bjj} - M_t)^2}{{\Gamma_t}^2}. \end{aligned} \quad (6.1)$$

While constraining the invariant masses of the leptonic W, and both the leptonic and hadronic top quarks to the true value in the simulation sample, 80.4 GeV/c^2 and 172.5 GeV/c^2, `MINUIT` runs to find the best jet to parton assignment with the smallest χ^2 varying the p_T of leading four jets and lepton, and the unclustered energy (UE) accordingly. The lepton p_T is varied within its uncertainty, $\sim 1\%$ of the p_T to be conservative. The uncertainty used for each jet p_T is obtained from the TS correction as described in the previous chapter 5. The unclustered energy (UE) is a negative vector sum of the MET, lepton, and all the reconstructed jets greater than 10 GeV/c including the leading four jets. Instead of varying the MET directly in the fitter, the UE is varied within 50% of the UE as an uncertainty.

In the jet-parton assignment, b-tagged jets are assigned to b-quarks. The b-quark that decayed directly from a top quark has a priority to have the b-tagged jet assigned. Thereby, in the two b-tagged jets event, both b-jets are assigned to the top quark decays, so that the di-jet mass are reconstructed from two un-tagged jets. When the event has three b-tagged jets, any two b-tagged jets are assigned to top-b-quark and one remained jet is assigned to $W/H^{\pm}$ based on minimum χ^2 for low mass $H^{\pm}$ ($\leq$ 120 GeV/c^2). However, for higher mass $H^{\pm}$ template the softer b-tagged jet is assigned to b-quark directly decaying from top quark hadronic side. Detail on this study is found in Sec. 6.3.

6.2 Goodness Cut

In principle, four jets assignment with lowest χ^2 is supposed to give the best di-jet mass distribution. However, the fitter is sometimes gone too bad and confuse the result with the best χ^2. Fig. 6.1 shows the unnatural tails in the di-jet mass distribution from the fitter chosen jet assignment. We develop a few conditions to reject certain combination that drive the fit to wrong way. Following criteria are required to be satisfied in selecting the best jet assignment along with the returned χ^2.

1. $|p_T^{\text{in}} - p_T^{\text{fitted}}| < 20$ GeV/c for each jet

2. M(hadronic top before mass constraint) < 200 GeV/c^2

First condition was driven from the $|p_T^{\text{fitted}} - p_T^{\text{input}}|$ comparing the correct assignment with the wrong assignment case. As seen in the Fig. 6.2, one jet from W and the hadronic side top-b-jet often vary the jet p_T too much when the jet assigns to wrong parton. Same symptom was observed in both SM $t\bar{t}$ and the $H^{\pm}$ signal $t\bar{t}$ samples. The first goodness cut avoids such cases.

While checking the kinematic distributions of the reconstructed $t\bar{t}$ events, we found that the wrong assignment used to have large hadronic top quark mass, M($b$jj) - the mass is reconstructed before the top mass constraint but using the same assignment given by the best χ^2 selection. In order to keep the correct assignment as much as possible, imposing an high-end cut on the M($b$jj) is tested in the Fig. 6.3. It turns out that the second goodness condition reject more wrong assignment case than applying the cut on $\chi^2 < 10$. Better di-jet

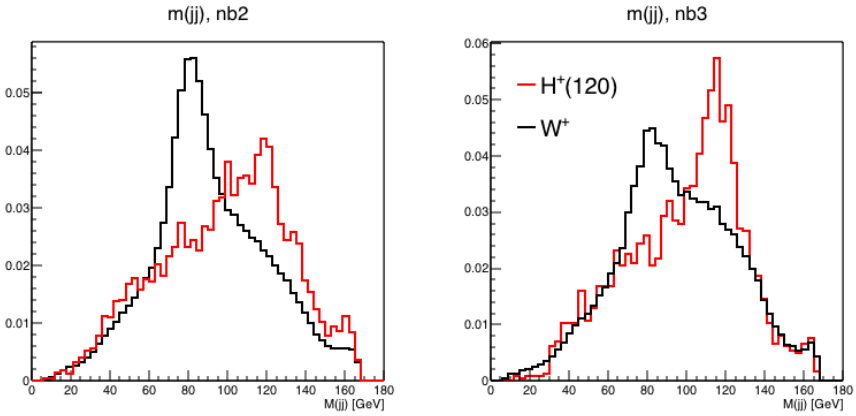

Figure 6.1: Di-jet invariant mass given from the lowest kinematic χ^2 fit. M(jj) from SM $t\bar{t}$ (black) and $H^{\pm}$ signal $t\bar{t}$ (red) is compared in two b-tagged (left) and three b-tagged (right) events. Events are normalized to unity.

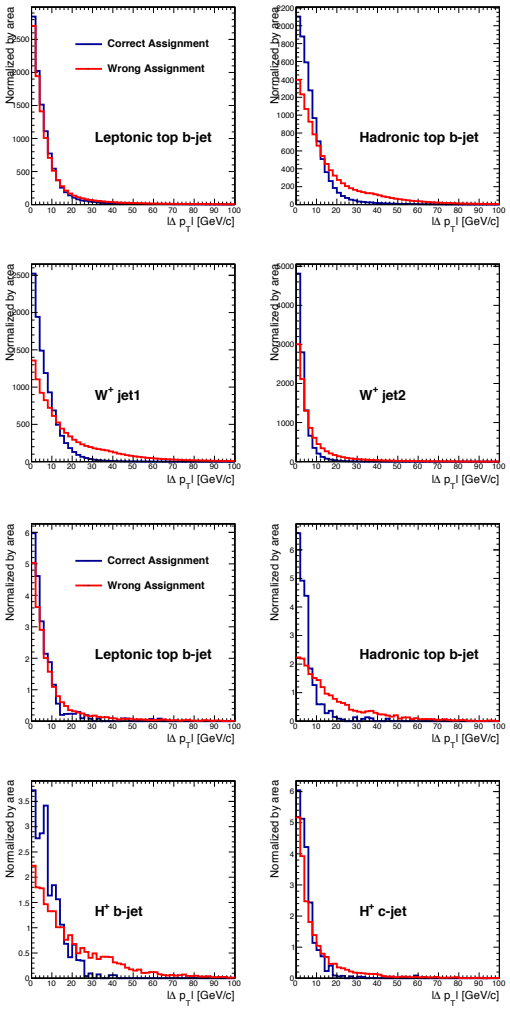

Figure 6.2: $|p_T^{\text{fitted}} - p_T^{\text{input}}|$ distributions from four jets in SM $t\bar{t}$ events (left four plots) and from the 150 GeV/c^2 $H^{\pm}$ $t\bar{t}$ events (right). The Δp_T for each jet assignment is compared in case of correct(dark blue)/wrong(red) assignment at the same time.

mass resolution is shown applying two goodness cuts in Fig. 6.4. Efficiency of the goodness cuts is estimated about 50% for SM $t\bar{t}$ and 60% for the $H^{\pm}$ signal $t\bar{t}$ sample.

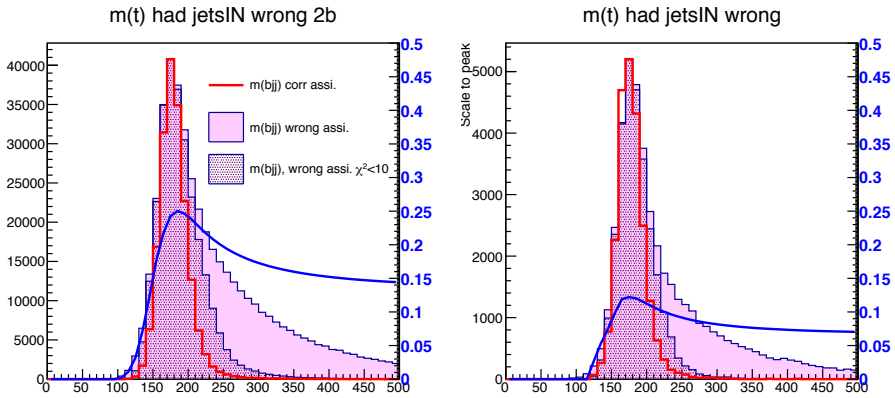

Figure 6.3: Hadronic side top quark mass distributions, M($b$jj), before χ^2 fit are compared between correct (red) and wrong (filled) assignment (with and without χ^2 cuts). Correct assignment fraction vs. upper M($b$jj) cut is overaid (blue line). Left plot is the M($b$jj) cut in two b-tag case and the right plot shows the same test in three b-tag events.

6.3 High $H^{\pm}$ mass fitter

The three b-quarks in the $H^{\pm}$ signal $t\bar{t}$ sample confuses the fitter with the wrong assignment that the b-quark from the $H^{\pm}$ assigned to the b-quark decaying from hadronic top quark, and vice versa. It is expected that the p_T distribution of the top-b-quark changes depending on the accompanying $H^{\pm}$ mass in the top quark decays. Fig. 6.5 compares the the generated p_T distribution of the top-b-quark in $H^{\pm}$ samples with the SM $t\bar{t}$ sample. As in the higher $H^{\pm}$ mass

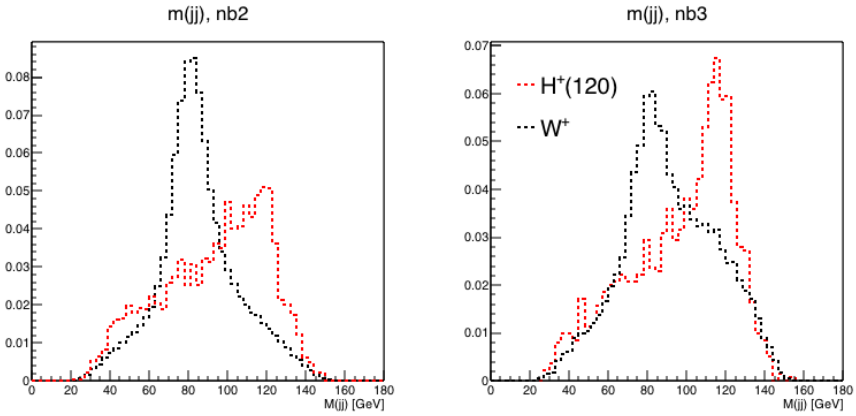

Figure 6.4: Di-jet invariant mass with the goodness cuts applied. M(jj) from SM $t\bar{t}$ (black) and $H^{\pm}$ signal $t\bar{t}$ (red) is compared in two b-tagged (left) and three b-tagged (right) events. Events are normalized to unity.

samples, the top-b-quark p_T used to be softer. Since there is no constraints on the di-jet mass, the fitter cannot pick the right solution when two b-jets are assigned to the same top quark and one b-jet p_T is softer than the others. It also affects the di-jet mass shape in the $H^{\pm}$ signal $t\bar{t}$ sample as shown in Fig. 6.6. In the top plot, using the normal reconstruction fitter, the di-jet mass from W and 100 GeV/c^2 $H^{\pm}$ reveals the expected shape except the 140 GeV/c^2 $H^{\pm}$ events. To get over the fit failure, the b-jet with smaller p_T is forced to be assigned to the top-b-quark. With this condition the signal di-jet mass shape is much recovered as seen in the bottom plot of Fig. 6.6. We use normal fitter for the $H^{\pm}$ mass of 90, 100, 110, and 120 GeV/c^2, and high mass fitter for 130, 140, 150 GeV/c^2 $H^{\pm}$ search.

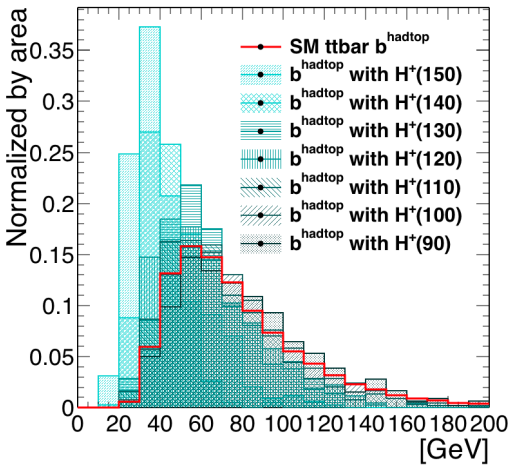

Figure 6.5: p_T distribution of the top-b-parton in the hadronic side top quark. The b-quark p_T distribution in the SM $t\bar{t}$ sample (red) is compared with the $H^{\pm}$ signal $t\bar{t}$ sample with M($H^{\pm}$) = 90, 100, 110, 120, 130, 140, and 150 GeV/c^2.

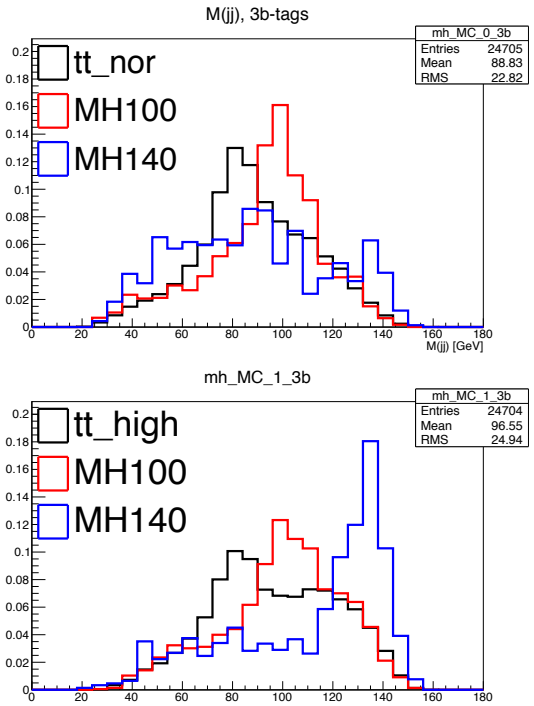

Figure 6.6: Di-jet mass distribution in the three b-tagged jets events with normal fitter (top) and high mass fitter (bottom). The distribution compares the W in SM $t\bar{t}$ with $H^{\pm}$ in the signal sample with M($H^{\pm}$) = 100, 140 GeV/c^2.

6.4 Kinematic Fitter Performance

By using the kinematic fitter for the SM $t\bar{t}$ and the $H^{\pm}$ signal samples, di-jet mass reconstruction can be significantly enhanced in terms of its shape. While the input variables of chi-square fitting being the jet pT with the Top Specific correction, the di-jet invariant mass from the fitter input-jets and the fitter output-jets are compared in order to confirm the kinematic fitter performance. Left plot of Fig. 6.7 shows di-jet mass reconstruction from the input-jets and the right plot is di-jet mass reconstruction from fitter output-jets for the SM $t\bar{t}$ with the normal fitter in three or more b-tagged jets events. Fig. 6.8 shows the same difference for $H^{\pm}$ mass 90 GeV/c^2, 100 GeV/c^2, 110 GeV/c^2, and 120 GeV/c^2 from the top plots to the bottom plots. Fig. 6.9 demonstrates the fitter performance for the high mass SM $t\bar{t}$, and Fig. 6.10 shows the fitter performance for the $H^{\pm}$ mass of 130 GeV/c^2, 140 GeV/c^2, and 150 GeV/c^2 from the top plots to the bottom ones.

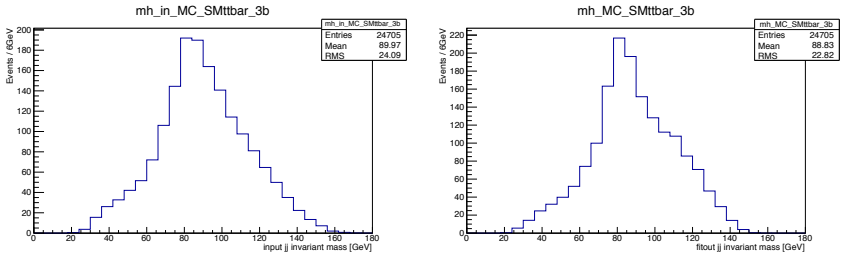

Figure 6.7: Mass reconstruction with kinematic fitter input jets (left), mass reconstruction with kinematic fitter output jets (right) in ≥ 3 b-jets events

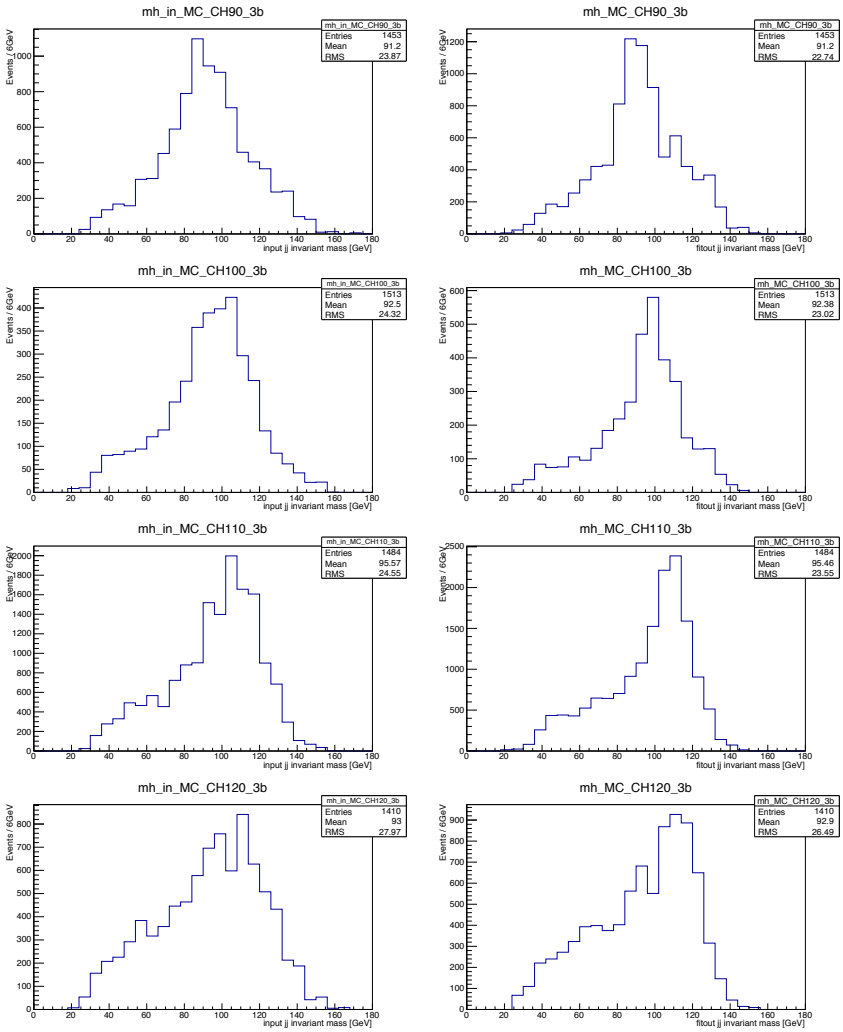

Figure 6.8: Mass reconstruction with kinematic fitter input jets (left), mass reconstruction with kinematic fitter output jets (right) in ≥ 3 b-jets events

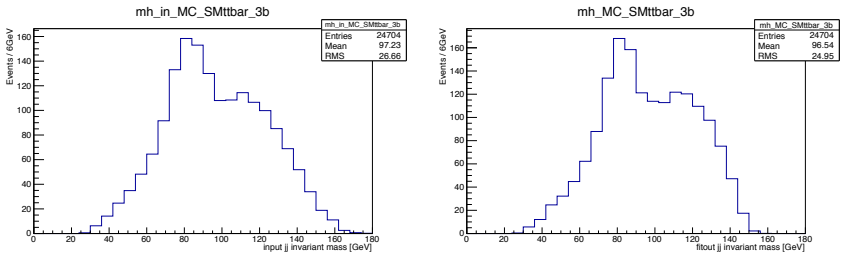

Figure 6.9: Mass reconstruction with high mass kinematic fitter input jets (left), mass reconstruction with high mass kinematic fitter output jets (right) in ≥ 3 b-jets events

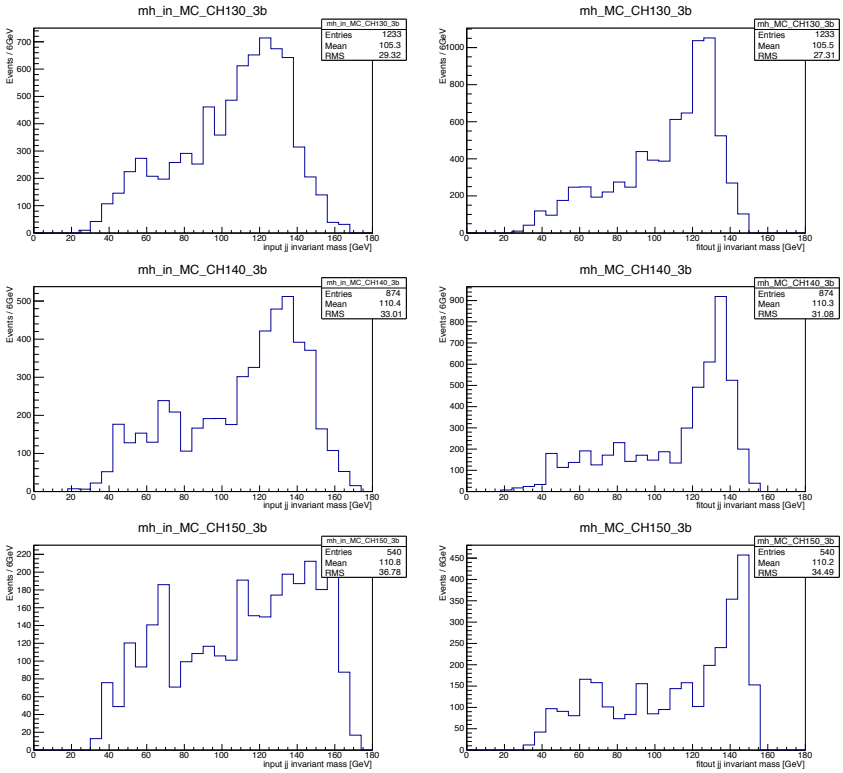

Figure 6.10: Mass reconstruction with high mass kinematic fitter input jets (left), mass reconstruction with high mass kinematic fitter output jets (right) in ≥ 3 b-jets events

6.5 Mass Template

Di-jet mass distributions in 2 b-tagged and 3 b-tagged region are prepared through the kinematic fitter described in previous subsection for the background MC samples and $H^{\pm}$ signal samples. In the 3 b-tagged region, the mass distribution from the low mass (≤ 120 GeV/c^2) fitter and the high mass fitter are obtained respectively, while in the 2 b-tagged region one common mass distribution is used.

Fig. 6.11 shows the 2 b-tags regions MC stack for the di-jet mass distribution for e+jets(left) and μ+jets(right) channels. Fig. 6.12 and Fig. 6.13 show the di-jet mass distributions in 3b-tags region from the normal fitter mass and the high mass fitter each. In Fig. 6.11, the signal $H^{\pm}$ shapes for 110 GeV/c^2 and 140 GeV/c^2 is drawn over the MC stacks, and the signal shapes are scaled that the branching ratio of top-quark to $H^{\pm}$ and bottom-quark is 0.2. In Fig. 6.12 and Fig. 6.13, the signal shapes over the MC stacks are scaled that the branching ratio of top-quark to $H^{\pm}$ and bottom-quark is 0.05, and the signal shapes are significant in 3b-tagged region.

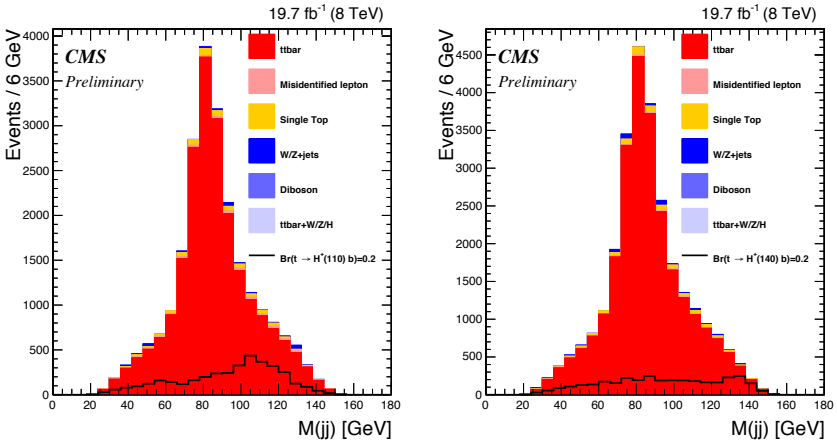

Figure 6.11: Di-jet mass distribution MC background stack in the two b-tagged jets events in e+jets(left) and μ+jets(right) channel. Di-jet mass distribution of $H^{\pm}$ signal sample with $H^{\pm}$ mass 110 GeV/c^2(140 GeV/c^2) are compared on top of the background stack.

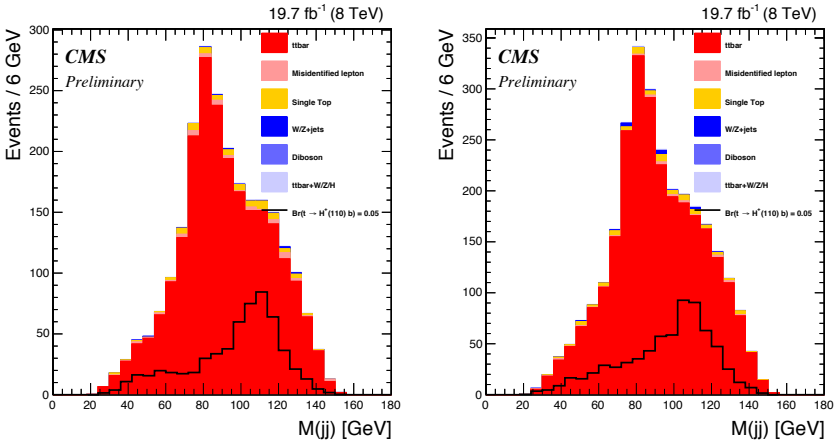

Figure 6.12: Di-jet mass distribution MC background stack in the three b-tagged jets events in e+jets(left) and μ+jets(right) channel with the normal fitter. Di-jet mass distribution of $H^{\pm}$ signal sample with $H^{\pm}$ mass 110 GeV/c^2 is compared on top of the background stack.

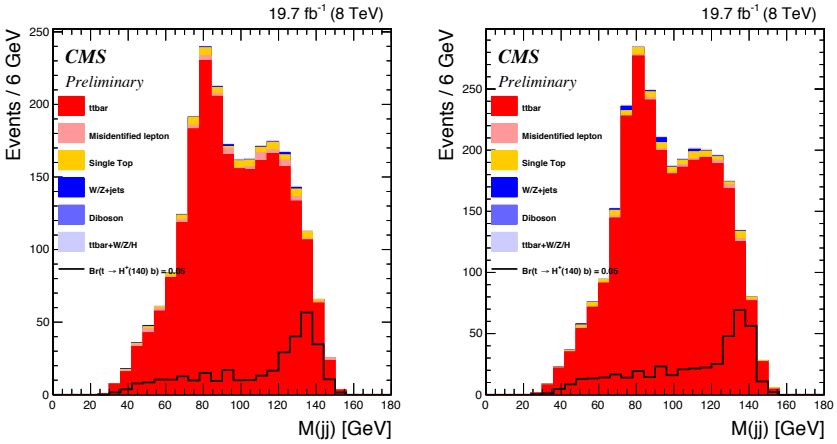

Figure 6.13: Di-jet mass distribution MC background stack in the three b-tagged jets events in e+jets(left) and μ+jets(right) channel with the high mass fitter. Di-jet mass distribution of $H^{\pm}$ signal sample with $H^{\pm}$ mass 140 GeV/c^2 is compared on top of the background stack.

Chapter 7

Systematic Uncertainty

The systematic uncertainties for this analysis are discussed below. There are two types of systematic uncertainties. The first one is related with overall rate of signal and background contribution. The second one is about the shape of the di-jet mass distribution. In this analysis, we use both 2 b-tag and 3 b-tag events. 2 b-tag events are dominated by background contributions, whereas the 3 b-tag region is more sensitive to signal events. Thus many common systematics between 2 b-tag and 3 b-tag samples can be constrained by high-statistics 2 b-tag data. This is one big advantage of using 2 b-tag sample in the analysis. The full list of systematic is given with detailed description below.

- **Jet energy scale (JES):** The JES uncertainty is one of the significant source of uncertainty in this analysis. Following the CMS prescription [14], JES uncertainty is evaluated as a function of jet p_T and η. The JES uncertainty affects both the event yield and the mass template shapes. In the events, jets are shifted by one standard deviation up and down, according to the p_T and η dependent JES uncertainty.

- **Jet energy resolution (JER):** As it is known that the jet energy resolution in data is measured to be poorer than the jet energy resolution in simulation, the jet energy resolution in the simulation sample is degraded in order to match the measurement in data. Thus, in order to estimate the uncertainty on the jet energy resolution, one standard deviation up and down with respect to the degraded resolution is applied.

- **B-tagging scale factor:** The b-tagging scale factor uncertainty has a dominant impact on this analysis in terms of rate systematic uncertainty because at least 2 b-tagged jets among the leading four jets are required. Also, in the 3 b-tags region, most SM $t\bar{t}$ events has at least one mis-tagged jet, which yields a large uncertainty in the 3b-tags region for the SM $t\bar{t}$. However, the b-tagging scale factor does not affect the di-jet invariant mass template.

- **Lepton identification/isolation/trigger scale factor:** For both e+jets and μ+jets channels, the uncertainty on the lepton identification and isolation efficiencies are estimated to be 0.2% (0.04%) for electron (muon) by applying one standard deviation up and down to the data/simulation scale factors. However, it is noted by POG group that the reference scale factor does not include systematic uncertainty of the tag-and-probe method. We assign 2% of rate uncertainty combining the ID/Iso scale factor uncertainty with trigger scale factor uncertainty (0.5%/0.04% for electron/muon), and consideration of the tag-and-probe systematic uncertainty.

- **Pile-up reweight:** The uncertainty on the pile-up reweight are calculated by applying one standard deviation up and down to the pile-up reweight scale factors.

- $t\bar{t}$ p_T**-reweight:** As the event-by-event weight is applied from the top p_T-reweight, it is thought that there is change in the shape due to top p_T-reweight. In order to estimate the shape difference, the shape is compared with and without top p_T-reweight being applied.

- $t\bar{t}$ **xsec:** The theoretical value of the $t\bar{t}$ cross section is used to estimate the backgrounds of the SM $t\bar{t}$ with 6.5% uncertainty. The calculation is done next-to-next-to leading order (NNLO) in QCD including resummation of next-to-next-to-leading logarithmic (NNLL) soft gluon terms. The PDF and α_S uncertainties are included in this uncertainty too. But this uncertainty may not be sufficient in 3 b-tags region, where there can an additional uncertainty in modeling of extra $b\bar{b}$ production. Thus, in 3 b-tag channel, we assign 15% uncertainty.

- **Top mass:** The top-quark mass is set to be 172.5 GeV/c^2 in this analysis, and we consider 1 GeV/c^2 variance for the top-quark mass. The uncertainty due to the top-quark mass variation is estimated by applying 1 GeV/c^2 up and down for the top-quark mass, the larger difference between the 1 GeV/c^2 up variance and the 1 GeV/c^2 down variance are taken as the uncertainty.

- **MC generator:** The Madgraph is the reference MC generator in this

analysis. The uncertainty due to the LO generator is estimated by using the $t\bar{t}$ sample generated by Powheg (NLO).

- **Flavour dependent JES:** The uncertainty on the detector response to the jet by its original parton flavour is estimated varying the jet p_T with given L5 uncertainty. The procedure is done by b-jet scale up/down while others same, and then repeated by varying other flavours up/down while b-quark jets stay still. This uncertainty also takes into account the difference in the hadronization processes given by PYTHIA and HERWIG.

- **Renormalization and factorization scales (Q2):** The uncertainty on the renormalization and factorization scales is estimated by the theory-inspired scale variations by factor of in 25% and 400% in $t\bar{t}$ events.

- **Matching between Matrix Element and Parton Showering:** The matching jet energy threshold that interfaces the matrix element (MADGRAPH) to the parton-showering (PYTHIA) is shifted by a factor of 0.5 and 2. We use $t\bar{t}$ sample with matching up/down to estimated the uncertainty.

- **QCD scale factor:** In estimating the QCD contribution by data-driven method, the QCD scale factors are derived. The QCD scale factor is defined to be the ratio of the number of QCD events(data-other MC samples) of between the lepton isolated region and the anti-isolated region where met is smaller than 20 GeV/c. The uncertainty of the QCD

scale factor are estimated by applying 200% and 50% of the original scale factors.

- **Luminosity Uncertainty:** The uncertainty on the luminosity measurement is given to be 2.6% by the Luminosity group.

The uncertainties on the scale factor does change the acceptance on the selection, however there is no effect given to the di-jet mass template. Thereby, the rate systematic uncertainties are estimated by counting the selected number of events with the $\pm$ 1 σ change, and summarized in Tab. 7.1, 7.2, 7.3, 7.4 for e+jets channel and in Tab. 7.5, 7.6, 7.7, 7.8 for μ+jets channel. Other uncertainties affect the di-jet mass distribution which corresponds to the shape difference by the $\pm$ 1 σ or up/down shift of the systematic factor. Except for the JES and JER, those uncertainties are closely related to the $t\bar{t}$ production, the dominant background as well as the mother of the $H^{\pm}$ signal process. For the $t\bar{t}$ systematic uncertainties, several samples, listed in Tab. 3.2, are processed and compared with the reference $t\bar{t}$ sample. Since there is no systematic sample for the $H^{\pm}$ signal $t\bar{t}$ event, the top and anti-top partons in the $H^{\pm}$ sample are weighted mimicking the top parton p_T distribution in the $t\bar{t}$ systematic samples. With this method, the $\pm$ 1 σ shift on the di-jet mass distribution are compared for Q^2, top mass, and MC generator uncertainty.

Table 7.1: List of rate systematic uncertainties of e+jets channel $H^{\pm}$ signal samples 2b-tags

$H^{\pm}$ mass (GeV/c^2)	90	100	110	120	130	140	150
2 b-tags							
B-tagging SF (b/c)	1.3%	1.2%	1.3%	1.2%	1.5%	1.6%	2.1%
B-tagging SF (light/gluon)	0.1%	0.1%	0.1%	0.2%	0.1%	0.1%	0.1%
Pile-up reweight SF	0.3%	0.8%	0.8%	0.1%	0.4%	0.4%	1.2%

Table 7.2: List of rate systematic uncertainties of e+jets channel $H^{\pm}$ signal samples 3b-tags

$H^{\pm}$ mass (GeV/c^2)	90	100	110	120	130	140	150
B-tagging SF (b/c)	5.7%	5.8%	5.7%	5.7%	5.7%	5.7%	5.6%
B-tagging SF (light/gluon)	0.3%	0.2%	0.2%	0.2%	0.3%	0.3%	0.7%
Pile-up reweight SF	0.6%	0.7%	0.3%	0.7%	0.5%	0.1%	0.7%

Table 7.3: List of rate systematic uncertainties of e+jets channel $t\bar{t}$ sample

	$t\bar{t}$(2b)	$t\bar{t}(3b_{nor})$	$t\bar{t}(3b_{high})$
B-tagging SF (b/c)	3.6%	5.7%	5.7%
B-tagging SF (light/gluon)	0.2%	2.8%	2.8%
Pile-up reweight SF	0.3%	0.3%	0.3%

Table 7.4: List of rate systematic uncertainties of e+jets channel non-$t\bar{t}$ samples

	non-$t\bar{t}(2b)$	non-$t\bar{t}(3b_{nor})$	non-$t\bar{t}(3b_{high})$
B-tagging SF (b/c)	3.0%	4.4%	4.3%
B-tagging SF (light/gluon)	1.7%	2.3%	2.3%
Pile-up reweight SF	0.7%	0.3%	0.4%

Table 7.5: List of rate systematic uncertainties of μ+jets channel $H^{\pm}$ signal samples 2b-tags

$H^{\pm}$ mass (GeV/c^2)	90	100	110	120	130	140	150
B-tagging SF (b/c)	1.3%	1.3%	1.2%	1.2%	1.4%	1.7%	2.1%
B-tagging SF (light/gluon)	0.1%	0.1%	0.1%	0.1%	0.1%	0.1%	0.1%
Pile-up reweight SF	0.4%	0.3%	0.2%	0.4%	0.1%	0.1%	0.2%

Table 7.6: List of rate systematic uncertainties of μ+jets channel $H^{\pm}$ signal samples 3b-tags

$H^{\pm}$ mass (GeV/c^2)	90	100	110	120	130	140	150
B-tagging SF (b/c)	5.7%	5.7%	5.8%	5.8%	5.7%	5.7%	5.7%
B-tagging SF (light/gluon)	0.3%	0.3%	0.3%	0.3%	0.2%	0.4%	0.4%
Pile-up reweight SF	0.4%	0.1%	0.1%	0.1%	0.3%	0.1%	0.4%

Table 7.7: List of rate systematic uncertainties of μ+jets channel $t\bar{t}$ sample

	non-$t\bar{t}$(2b)	non-$t\bar{t}$(3b$_{\mathrm{nor}}$)	non-$t\bar{t}$(3b_{high})
B-tagging SF (b/c)	3.6%	5.7%	5.7%
B-tagging SF (light/gluon)	0.2%	2.7%	2.7%
Pile-up reweight SF	0.5%	0.7%	0.7%

Table 7.8: List of rate systematic uncertainties of μ+jets channel non-$t\bar{t}$ samples

	non-$t\bar{t}$(2b)	non-$t\bar{t}$(3b$_{\mathrm{nor}}$)	non-$t\bar{t}$(3b_{high})
B-tagging SF (b/c)	2.9%	4.0%	4.0%
B-tagging SF (light/gluon)	1.9%	3.2%	3.2%
Pile-up reweight SF	1.3%	0.4%	0.3$

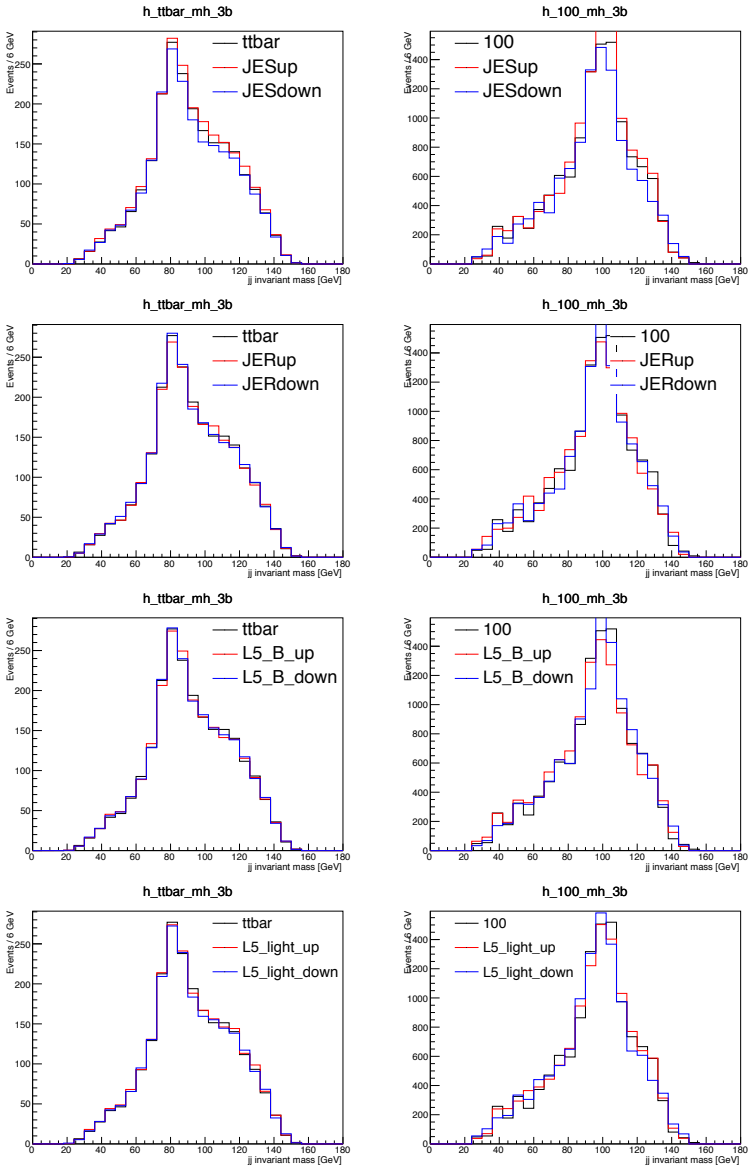

Figure 7.1: Systematic uncertainties for di-jet mass reconstruction of the Standard Model $t\bar{t}$ (left), and for charged Higgs signal at 100 GeV/c^2 (right) in 3 b-tags e+jets channel for low mass fitter: showing shape uncertainties due to jet energy scale, jet energy resolution, L5 b-quark uncertainty, and L5 other flavored quark uncertainty from top plots toward bottom plots

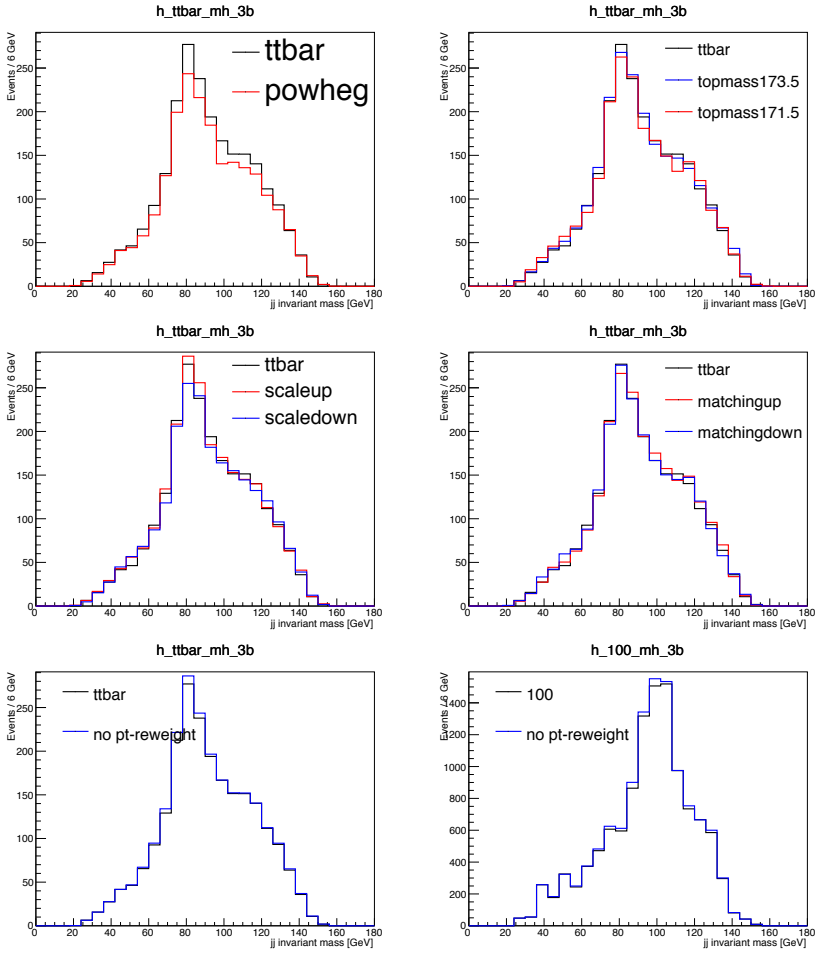

Figure 7.2: $t\bar{t}$ Systematic uncertainties for di-jet mass reconstruction of the Standard Model $t\bar{t}$ (left) in 3 b-tag e+jets channel for low mass fitter, showing shape uncertainties due to MC generator, top quark mass, Q^2 scale, ME-matching, and p_T-reweight for $t\bar{t}$ and $H^{\pm}$ (100 GeV/c^2) from top plots toward the bottom plots.

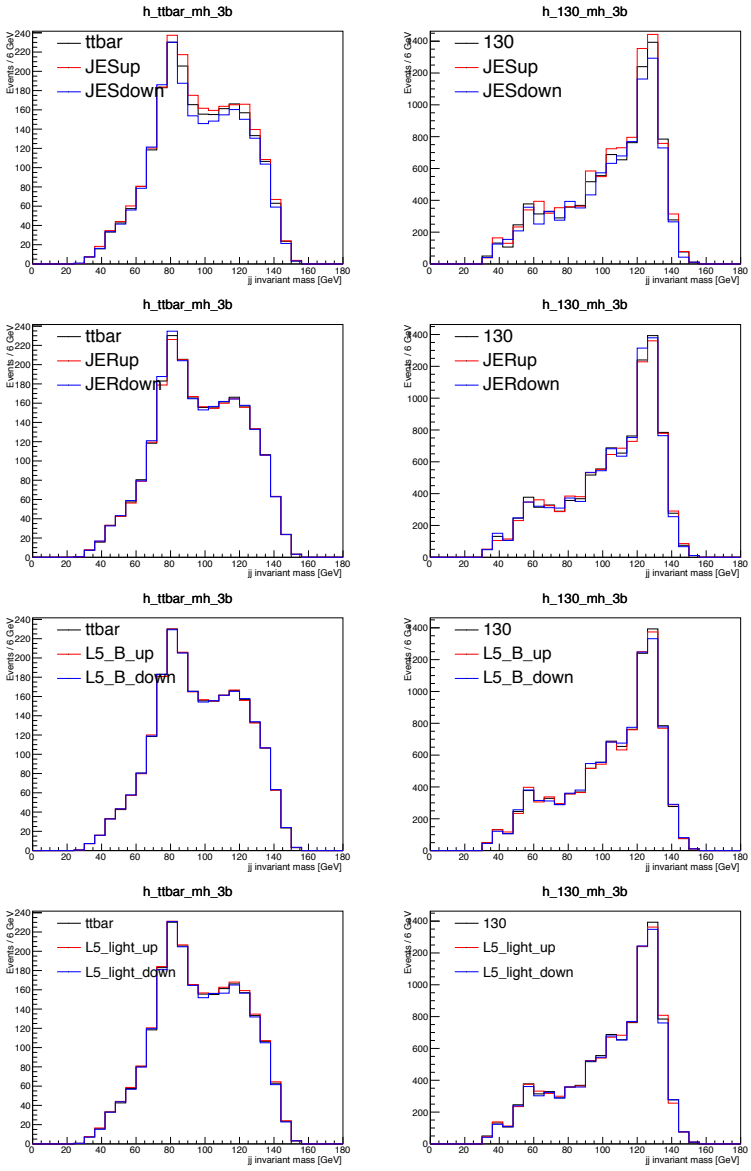

Figure 7.3: Systematic uncertainties for di-jet mass reconstruction of the Standard Model $t\bar{t}$ with high mass fitter(left) and of charged Higgs signal at 130 GeV/c^2 with high mass fitter(right) in 3 b-tag e+jets channel, jet energy scale, jet energy resolution, L5 b-quark uncertainty, and L5 other flavored quark uncertainty from top plots toward the bottom plots

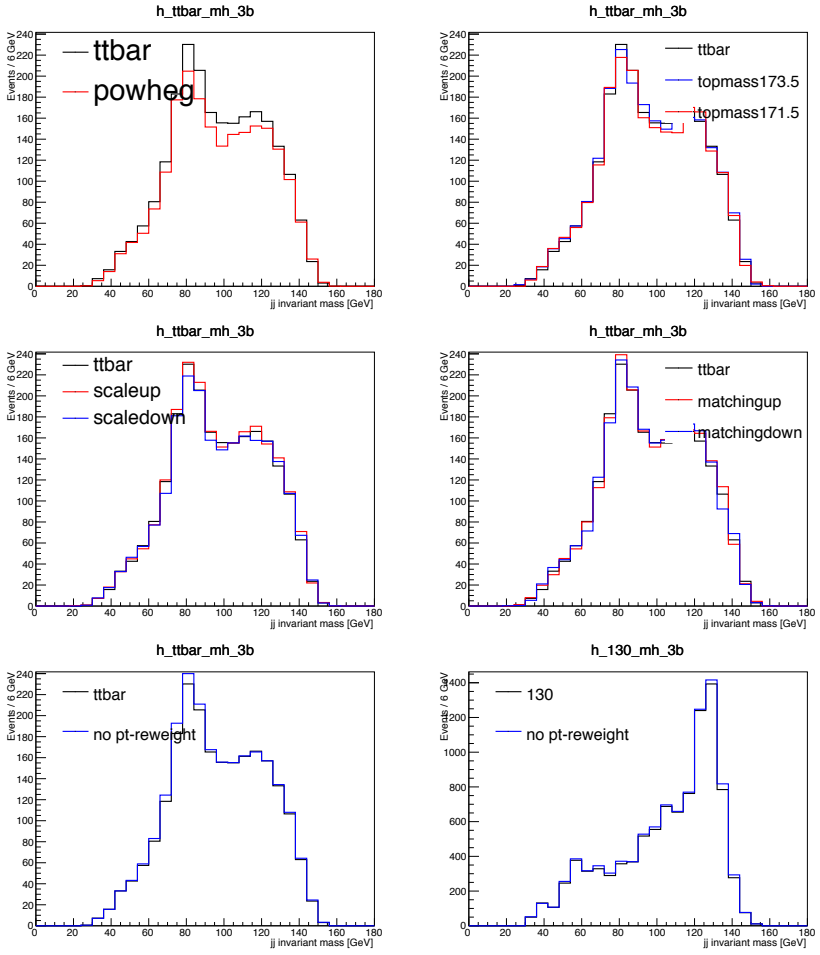

Figure 7.4: $t\bar{t}$ Systematic uncertainties for di-jet mass reconstruction of the Standard Model $t\bar{t}$ (left) in 3 b-tag e+jets channel for high mass fitter, showing shape uncertainties due to MC generator, top quark mass, Q^2 scale, ME-matching, and p_T-reweight for $t\bar{t}$ and $H^{\pm}$ (130 GeV/c^2) from top plots toward the bottom plots.

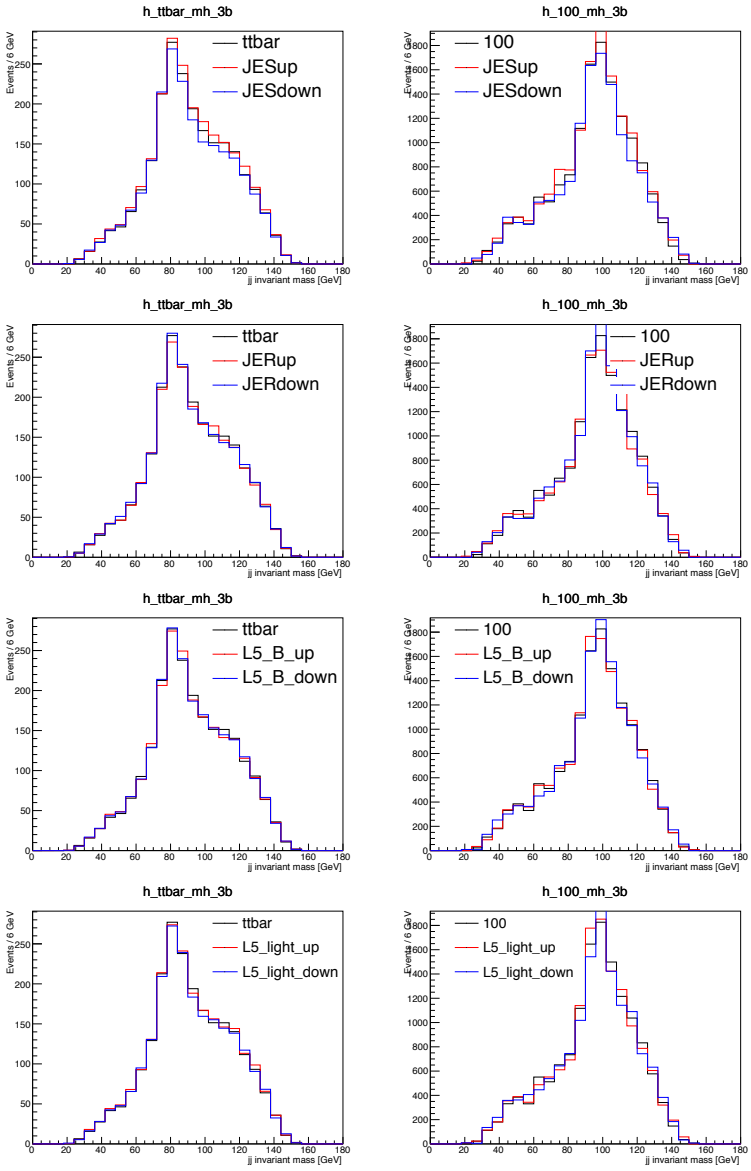

Figure 7.5: Systematic uncertainties for di-jet mass reconstruction of the Standard Model $t\bar{t}$ (left) and for charged Higgs signal at 100 GeV/c^2 (right) in 3 b-tags e+jets channel for low mass fitter: template shifts due to jet energy scale, jet energy resolution, L5 b-quark uncertainty, and L5 other flavored quark uncertainty from top plots toward the bottom plots.

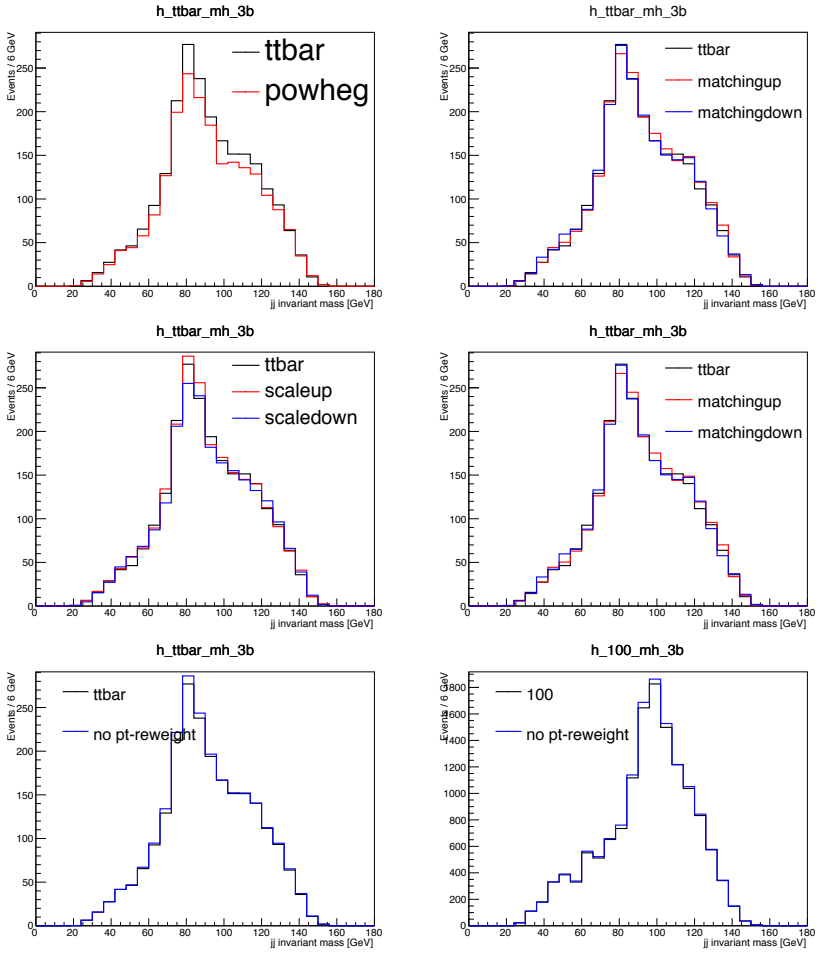

Figure 7.6: $t\bar{t}$ Systematic uncertainties for di-jet mass reconstruction of the Standard Model $t\bar{t}$ (left) in 3 b-tag e+jets channel for low mass fitter, showing shape uncertainties due to MC generator, top quark mass, Q^2 scale, ME-matching, and p_T-reweight for $t\bar{t}$ and $H^{\pm}$ (100 GeV/c^2) from top plots toward the bottom plots.

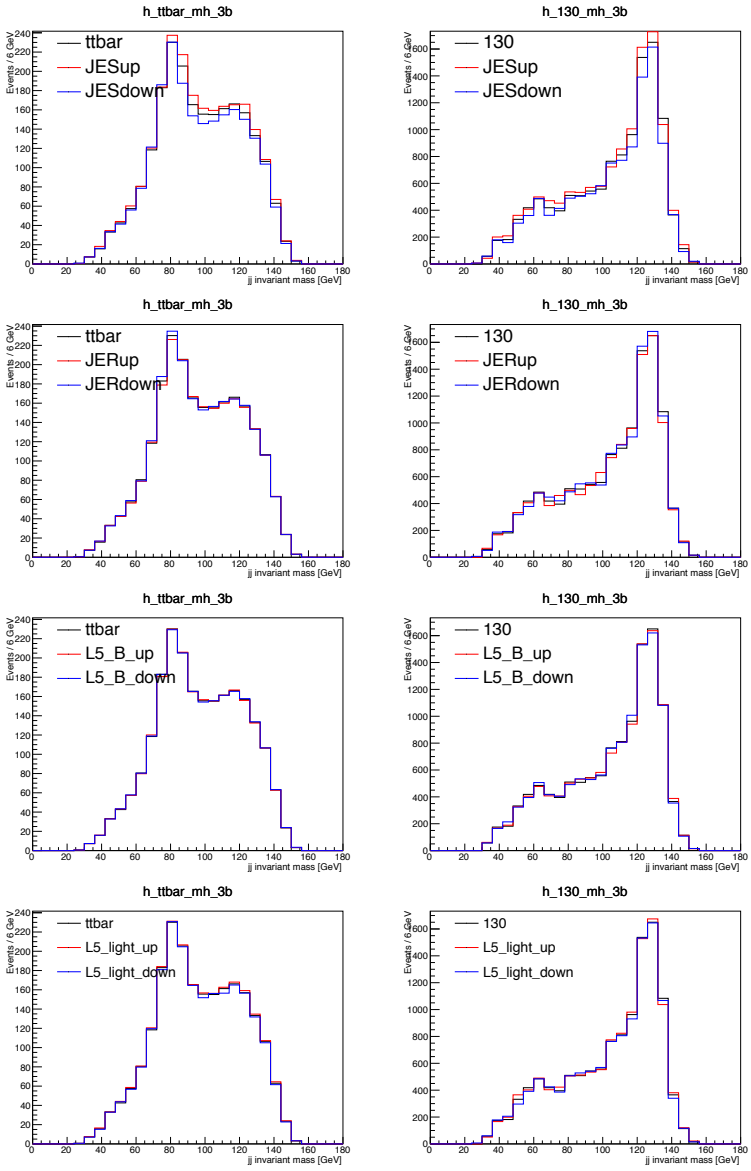

Figure 7.7: Systematic uncertainties for di-jet mass reconstruction of the Standard Model $t\bar{t}$ with high mass fitter(left) and of charged Higgs signal at 130 GeV/c^2 with high mass fitter(right) in 3 b-tag e+jets channel, jet energy scale, jet energy resolution, L5 b-quark uncertainty, and L5 other flavored quark uncertainty from top plots toward the bottom plots

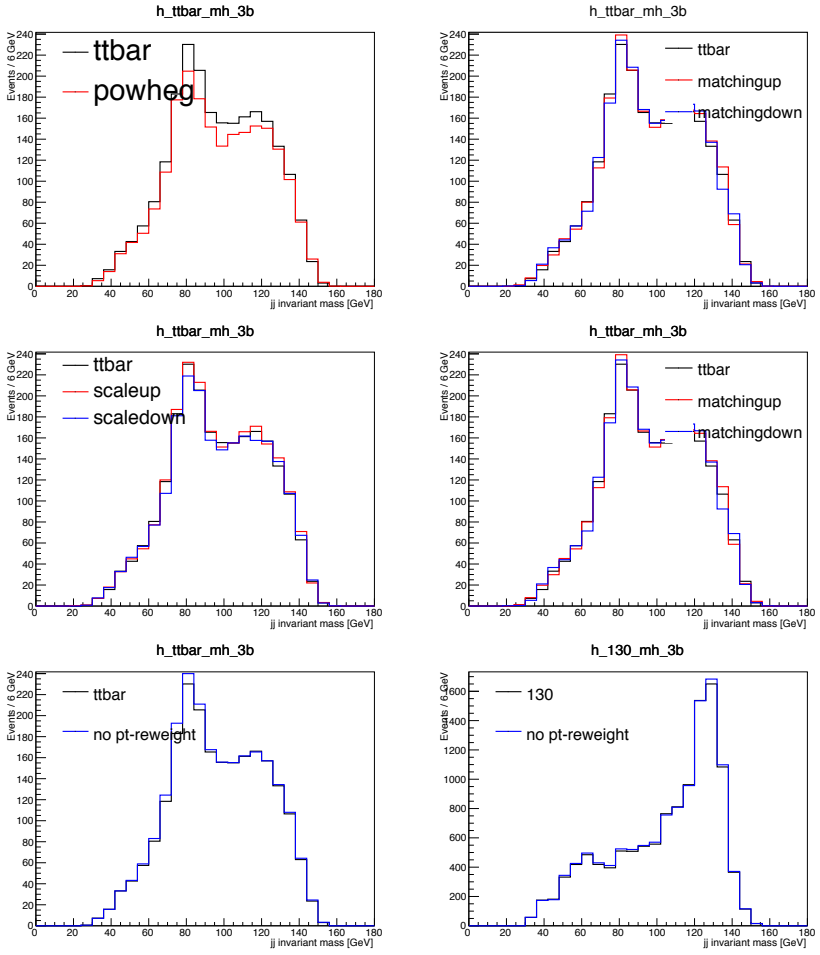

Figure 7.8: $t\bar{t}$ Systematic uncertainties for di-jet mass reconstruction of the Standard Model $t\bar{t}$ (left) in 3 b-tag e+jets channel for high mass fitter, showing shape uncertainties due to MC generator, top quark mass, Q^2 scale, ME-matching, and p_T-reweight for $t\bar{t}$ and $H^{\pm}$ (130 GeV/c^2) from top plots toward the bottom plots.

Chapter 8

Fit on B($t \to H^{\pm}b$)

`RooStat` based statistics tools (`Combine`) [3] are used for this shape analysis. The templates are prepared from the $t\bar{t}$ kinematic fitter in 2 b-tag and 3 b-tag region respectively as shown in Sec. 6.5. The 3 b-tagged events template shape is very sensitive in the $H^{\pm}$ signal hunt because of the higher acceptance from $H^{\pm}$ which has an additional b-quark in the final state. However, due to the low statistics in the 3 b-tagged region, we simultaneously fit the 2 b-tagged events to have reliable result.

8.1 Upper limit on B($t \to H^{\pm}b$) at 95% CL with Stat. Error

The upper limit on decay branching ratio of top quark (B($t \to H^{\pm}b$)) with 95% confidence level is obtained by using Asymptotic fit on the templates. Limits for e+jets channel are calculated separately in 2 b-tagged and 3 b-tagged regions as seen in Fig. 8.1. The limit from 2 b-tags fit is about 1% and from 3 b-tags fit is 0.5% level. Similar limit is estimated from μ+jets channel

in Fig. 8.2. When those two regions are fit simultaneously, the limit goes down to ∼0.3% of the B($t \to H^{\pm}b$).

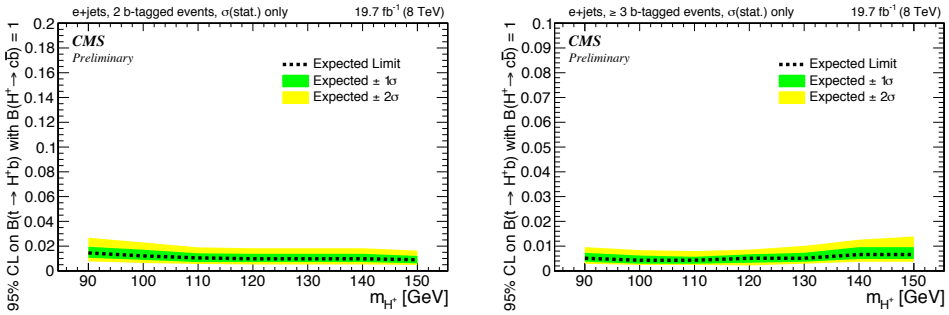

Figure 8.1: Upper limit on B($t \to H^{\pm}b$) with 95% C.L. for electron channel, 2 b-tags (left) and 3 b-tags (right) template fit respectively. No systematic uncertainty included.

8.2 Upper limit on B($t \to H^{\pm}b$) at 95% CL with Syst. Error

The upper limit on B($t \to H^{\pm}b$) with 95% confidence level is obtained including all the systematic uncertainties estimated previously in Sec. 7. By adding systematic errors, as seen in Fig. 8.4 and Fig. 8.5 for e and μ channel, the limits goes up twice of the limit with statistical uncertainty only. It implies that this analysis is heavily affected by the systematic uncertainties. In combination of 2 b-tags and 3 b-tags events the upper limit is obtained nearly 1% in Fig. 8.6.

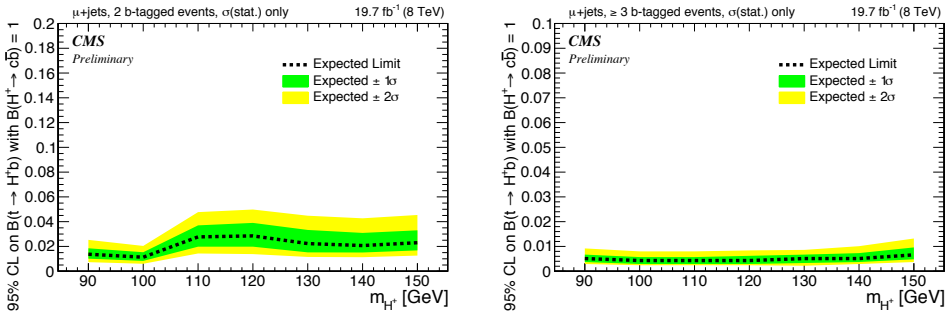

Figure 8.2: Upper limit on B($t \to H^{\pm}b$) with 95% C.L. for muon channel, 2 b-tags (left) and 3 b-tags (right) template fit respectively. No systematic uncertainty included.

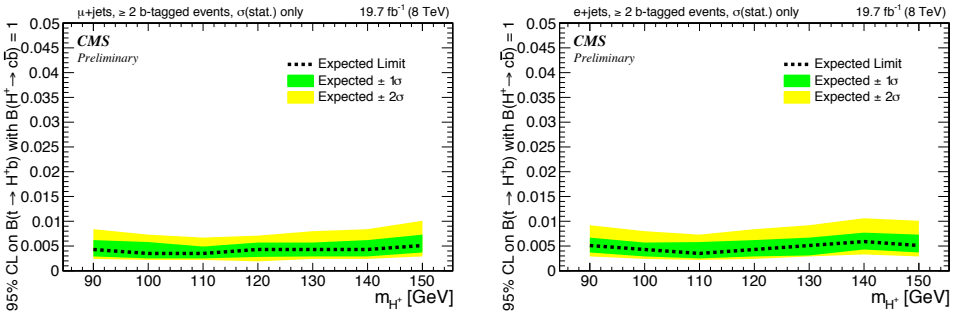

Figure 8.3: Upper limit on B($t \to H^{\pm}b$) with 95% C.L. for combined (2 b-tags & 3 b-tags) fit for muon (left) and electron channel (right) respectively. No systematic uncertainty included.

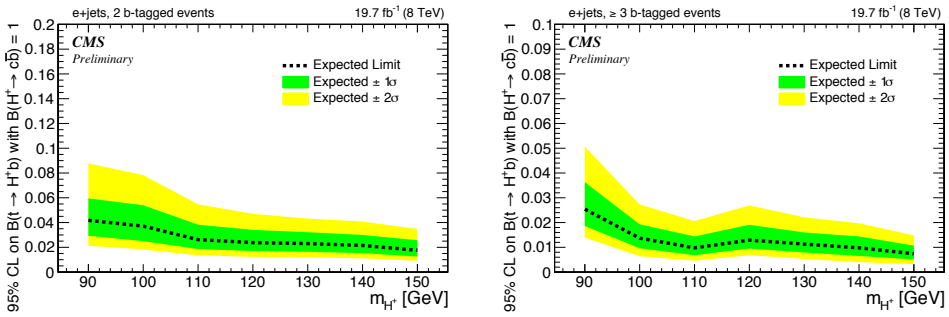

Figure 8.4: Upper limit on B($t \to H^{\pm}b$) with 95% C.L. for electron channel, 2 b-tags (left) and 3 b-tags (right) template fit respectively. All systematic uncertainties included.

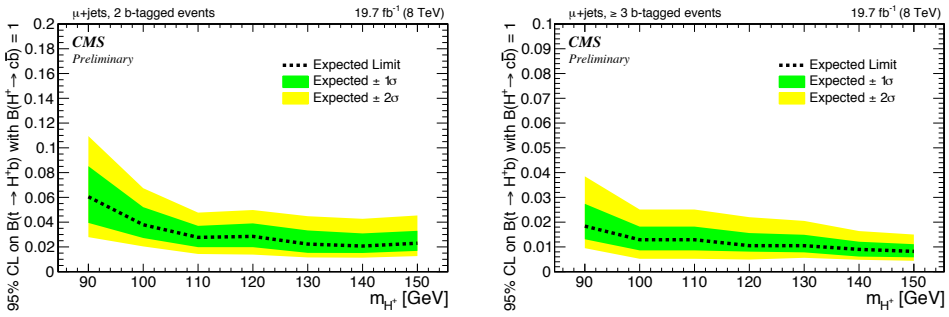

Figure 8.5: Upper limit on B($t \to H^{\pm}b$) with 95% C.L. for muon channel, 2 b-tags (left) and 3 b-tags (right) template fit respectively. All systematic uncertainties included.

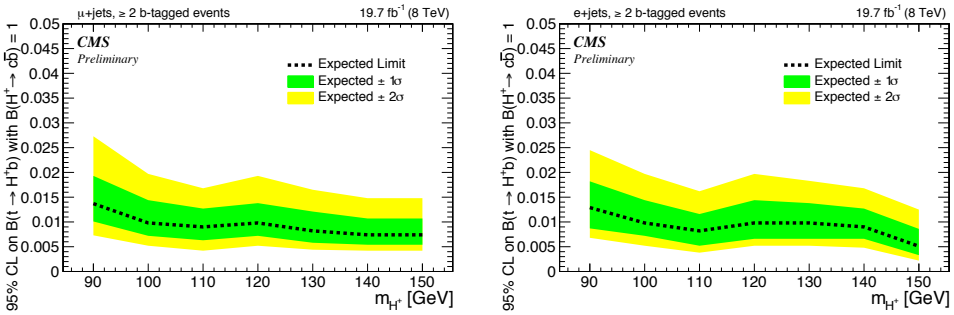

Figure 8.6: Upper limit on B($t \to H^{\pm} b$) with 95% C.L. for combined (2 b-tags & 3 b-tags) fit for muon (left) and electron channel (right) respectively. All systematic uncertainties included.

Chapter 9

Result and Summary

This analysis looks for a Higgs boson with single charge from $t\bar{t}$ decays in lepton+jets channel. It is the first attempt to search for the charged Higgs decaying to cb, thereby one additional b-jet is expected in the final state. By using the $t\bar{t}$ kinematic template fit, leptonically decayed W and top quarks are constrained by PDG W and top quark mass (=172.5 GeV/c^2 in this study) while the di-jet invariant mass reveals the mass of boson. Here in this note, the di-jet mass is fitted based on the SM $t\bar{t}$, $H^{\pm}$, and non-$t\bar{t}$ SM backgrounds template in 2 b-tags and 3 b-tags separately. Assuming no excess over SM W mass, the upper limits on B($t \to H^{\pm}b$) with 95% confidence level are obtained in Fig. 9.1 with and without the systematic uncertainties being included. Fig. 9.2 shows the observed result in muon channel and electron channel respectively, Fig. 9.3 shows the observed result where both channels are combined. In Fig. 9.3, the observed limit seems larger than expected limit in low mass region of $H^{\pm}$. Further study for systematic uncertainties and limit calculation is on-going.

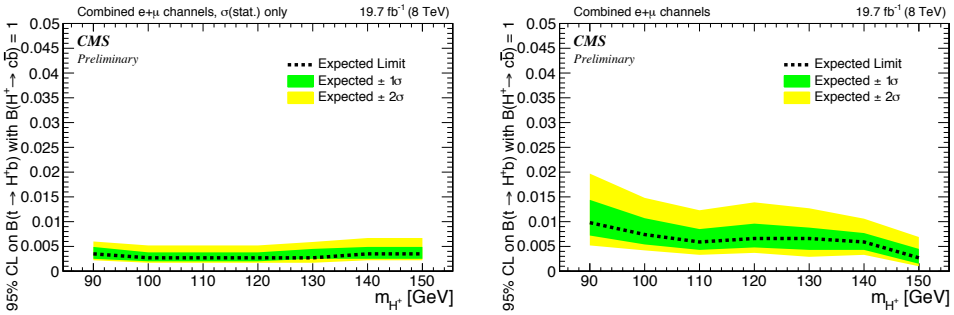

Figure 9.1: Upper limit on B($t \to H^{\pm}b$) with 95% C.L. in combination of electron and muon channel. Limit with statistical uncertainty only seen on left and the limit with all systematic uncertainties shown on right.

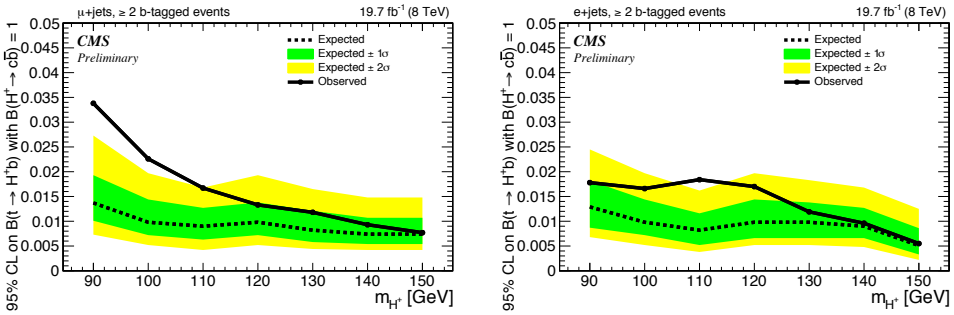

Figure 9.2: Upper limit on B($t \to H^{\pm}b$) with 95% C.L. for combined (2 b-tags & 3 b-tags) fit for muon (left) and electron channel (right) respectively. All systematic uncertainties included. The result from data is overlaid.

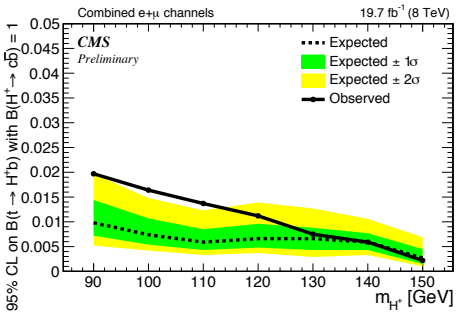

Figure 9.3: Upper limit on B($t \to H^{\pm}b$) with 95% C.L. in combination of electron and muon channel. The result from data is overlaid.

Bibliography

[1] A. Abulencia *et al.* Search for charged Higgs bosons from top quark decays in $p\bar{p}$ collisions at $\sqrt{s} = 1.96$ TeV. *Phys. Rev. Lett*, 96:042003, 2006.

[2] A. Salam. Weak and electromagnetic interactions. In N. Svartholm, editor, 8^{th} *Nobel Symposium.* Almqvist and Wiksell, Stockholm, 1968.

[3] Andrew Gilbert *et al.* Documentation of the roostats-based statistics tools for higgs pag. Cms twiki.

[4] CMS Collaboration. Commissioning of the particle-flow reconstruction in minimum-bias and jet events from *pp* collisions at 7 tev. CMS Physics Analysis Summary CMS-PAS-PFT-10-002, 2010.

[5] CMS Collaboration. Electron reconstruction and identification at $\sqrt{s} =$ 7 tev. CMS Physics Analysis Summary CMS-PAS-EGM-10-004, 2010.

[6] CMS Collaboration. Performance of muon identification in *pp* collisions at $\sqrt{s} = 7$ tev. CMS Physics Analysis Summary CMS-PAS-MUO-10-002, 2010.

[7] CMS Collaboration. Jet energy scale and resolution in the 8 tev *pp* data. CMS Physics Analysis Summary CMS-PAS-JME-13-004, 2013.

[8] ATLAS Collaboration. Observation of a new particle in the search for the standard model higgs boson with the atlas detector at the lhc. *Phys. Lett. B*, 716:1, 2012.

[9] ATLAS Collaboration. Search for charged Higgs bosons decaying via $H^{\pm} \to \tau^{\pm}\nu$ in top quark pair events using pp collision data at $\sqrt{s} = 8$ TeV with the ATLAS detector. *JHEP*, 2012:039, 2012.

[10] ATLAS Collaboration. Measurements of higgs boson production and couplings in diboson final states with the atlas detector at the lhc. *Phys. Lett. B*, 726:88, 2013.

[11] ATLAS Collaboration. Search for a light charged Higgs boson in decays of channel $H^{+} \to c\bar{s}$ in $t\bar{t}$ events using *pp* collision data at $\sqrt{s} = 7$ TeV with the ATLAS detector. *Eur. Phys. J. C*, 73:2465, 2013.

[12] ATLAS Collaboration. Search for charged Higgs bosons decaying via $H^{\pm} \to \tau^{\pm}\nu$ in fully hadronic final states using pp collision data at $\sqrt{s} =$ 8 TeV with the ATLAS detector. *JHEP*, 2015:088, 2015.

[13] CDF Collaboration. Search for charged Higgs bosons in decays of top quarks in $p\bar{p}$ collisions at $\sqrt{s} = 1.96$ TeV. *Phys. Rev. Lett*, 103:101803, 2009.

[14] CMS Collaboration. Determination of jet energy calibration and transverse momentum resolution in cms. *JINST*, 6:P11002, 2011.

[15] CMS Collaboration. Missing transverse energy performance of the cms detector. *JINST*, 6:09001, 2011.

[16] CMS Collaboration. Observation of a new boson at a mass of 125 gev with the cms experiment at the lhc. *Phys. Lett. B*, 716:30, 2012.

[17] CMS Collaboration. Identification of b-quark jets with the cms experiment. *JINST*, 8:P04013, 2013.

[18] CMS Collaboration. Observation of a new boson with mass near 125 gev in pp collisions at $\sqrt{s} = 7$ and 8 tev. *JHEP*, 06:081, 2013.

[19] CMS Collaboration. Search for a light charged higgs boson decaying to cs in pp collisions at $\sqrt{s} = 8$ tev. *JHEP*, 12:178, 2015.

[20] D0 Collaboration. Search for charged Higgs bosons in top quark decays. *Phys. Lett. B*, 11:016, 2009.

[21] G. Branco *et al.* Theory and phenomenology of two-Higgs-doublet models. *Phys. Rept.*, 516:1, 2012.

[22] J. Alwall, M. Herquet, and F. Maltoni. Madgraph 5: going beyond. *JHEP*, 06:128, 2011.

[23] J. F. Gunion, H. E. Harber, G. Kane, and S. Dawson. In *The Higgs Hunter's Guide*. Westview Press, 2000.

[24] M. Cacciari, G. P. Salam, and G. Soyez. The anti-k_t jet clustering algorithm. *JHEP*, 04:063, 2008.

[25] S. Alioli *et al.* A general framework for implementing nlo calculations in shower monte carlo programs: the powheg box. *JHEP*, 06:043, 2010.

[26] S. Chatrchyan *et al.* Search for a light charged Higgs boson in top quark decays in pp collisions at $\sqrt{s} = 7$ TeV. *JHEP*, 2012:143, 2012.

[27] S. L. Glashow. Partial-Symmetries of weak interactions. *Nucl. Phys.*, 22:579, 1961.

[28] S. L. Glashow, J. Iliopoulos, and L. Maiani. Weak Interactions with Lepton-Hadron Symmetry. *Nucl. Phys.*, 2:1285, 1970.

[29] J. Hernandez-Sanchez S. Moretti, A.G. Akeroyd. $h^{\pm} \to cb$ in models with two or more higgs doublets. *arXiv*, 1409.7596, hep-ph.

[30] S. Weinberg. A Model of Leptons. *Phys. Rev. Lett.*, 19:1264, 1967.

[31] T. Sjőstrand, S. Mrenna, and P. Skands. Pythia 6.4 physics and manual. *JHEP*, 05:026, 2006.

[32] V. Khachatryan *et al.* Search for a light charged Higgs boson decaying to $c\bar{s}$ in pp collisions at $\sqrt{s} = 8$ TeV. *JHEP*, 2015:178, 2015.

[33] V. M. Abazov *et al.* Search for charged Higgs bosons in decays of top quarks. *Phys. Rev. D*, 80:051107, 2009.

Appendix A

Appendix

A.1 Measurements of Jet Response and its Uncertainty

Plots here shows the Gaussian fitting result on the jet p_T responses in each pt region of a charm quark jet (Fig. A.1) and of a light flavoured quark jet (Fig. A.2. Both jet response is measured in central delector region of $|\eta| < 0.174$. The responses within same p_T range but in different pseudo-rapidity are shown in Fig. A.3 for c-quark jet and in Fig. A.4 for light flavoured jet. Uncertainties on this measurement are taken as a width of the Gaussian fit and parameterized as a function of p_T as seen in Fig. A.5 and in Fig. A.6.

A.2 Mass Templates: $H^{\pm}$ vs $W^{\pm}$ in $t\bar{t}$

The template of $H^{\pm}$ is compared with W in a normalized shape in Fig. A.7 for $H^{\pm}$ mass of 90 to 120 GeV/c^2 and in Fig. A.8 for $H^{\pm}$ mass of 130 to 150 GeV/c^2.

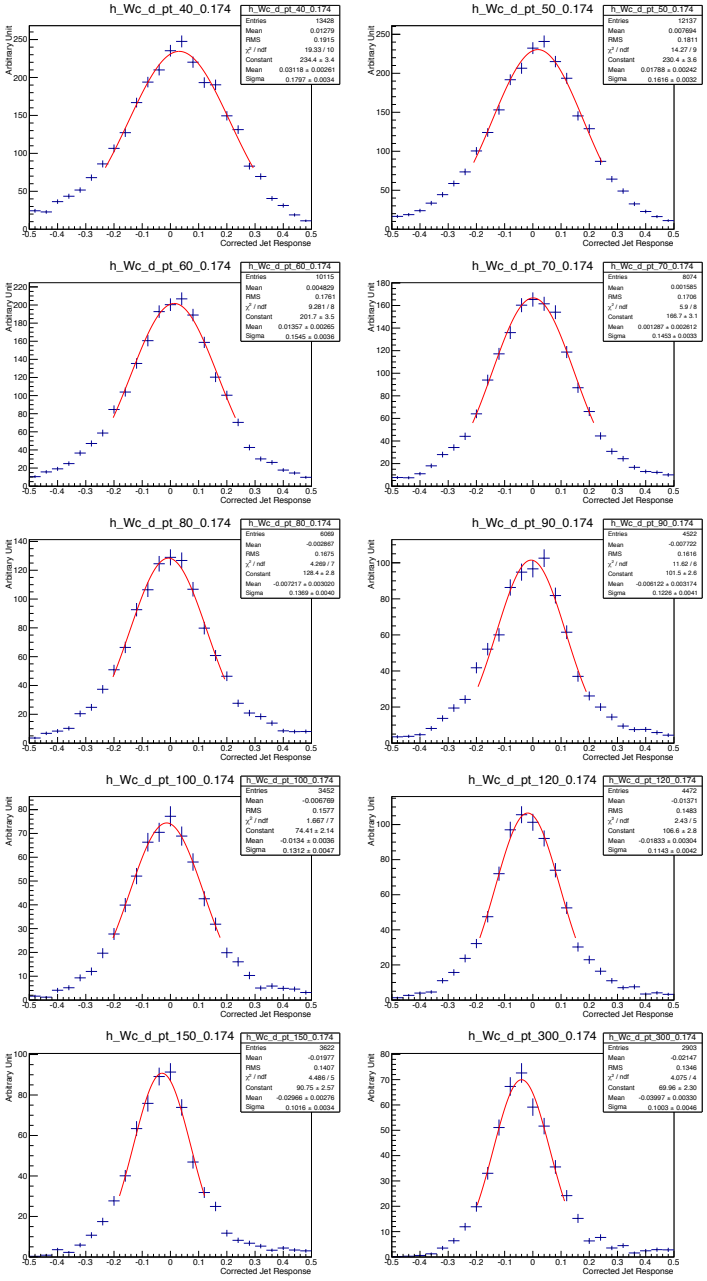

Figure A.1: Corrected pT response distributions for c-quark jet where $|\eta|$ is smaller than 0.174

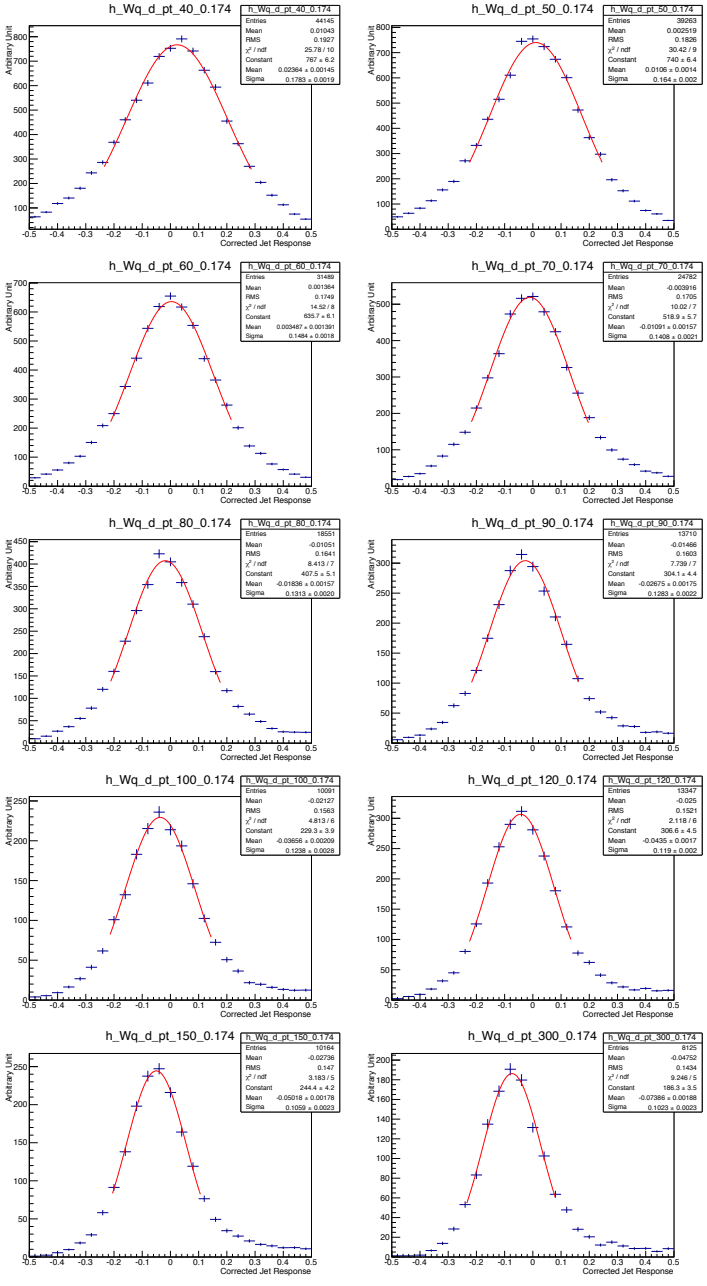

Figure A.2: Corrected pT response distributions for light-flavour jet where $|\eta|$ is smaller than 0.174

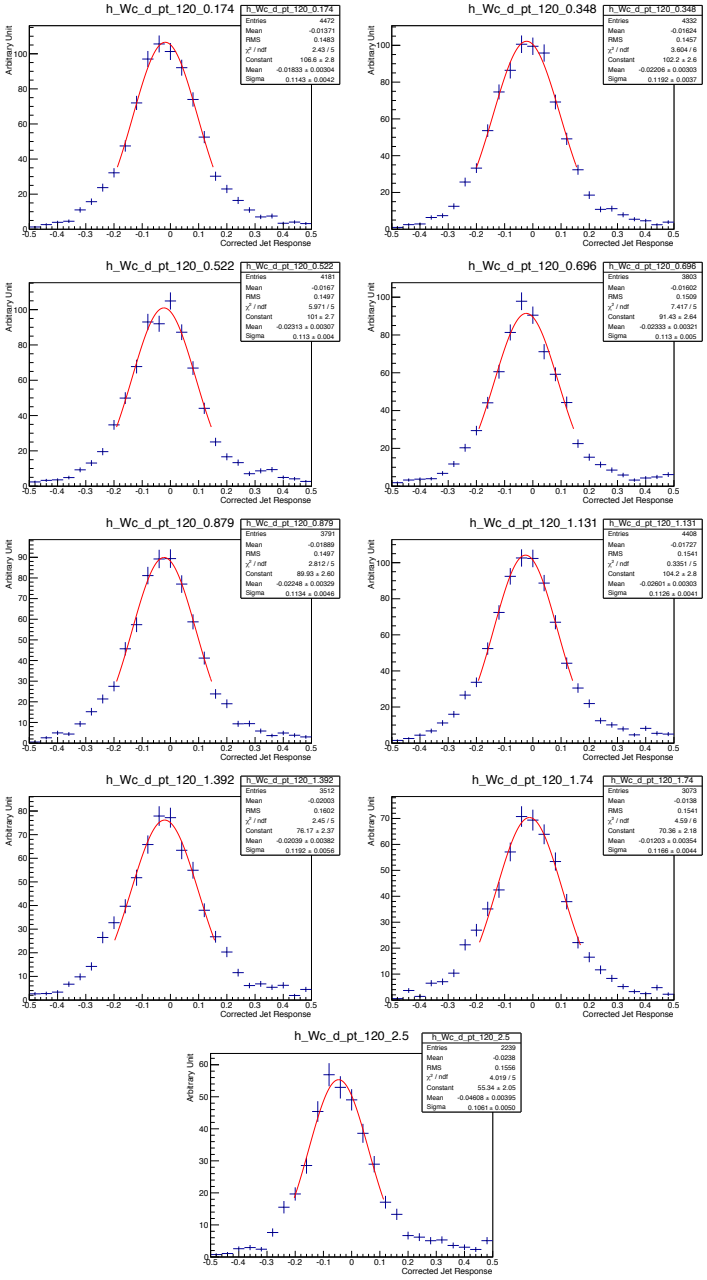

Figure A.3: Corrected pT response distributions for c-quark jet where jet pT is between 100 GeV/c^2 to 120 GeV/c^2.

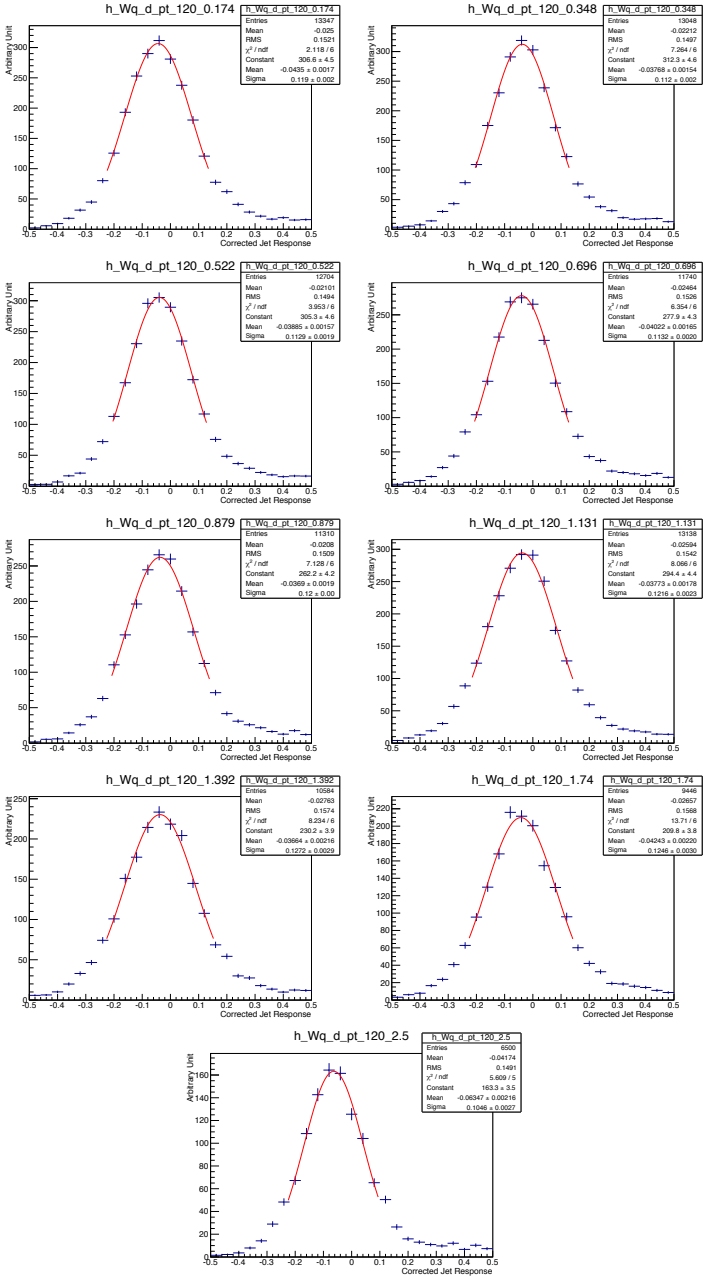

Figure A.4: Corrected pT response distributions for light-flavour jet where jet pT is between 100 GeV/c^2 to 120 GeV/c^2.

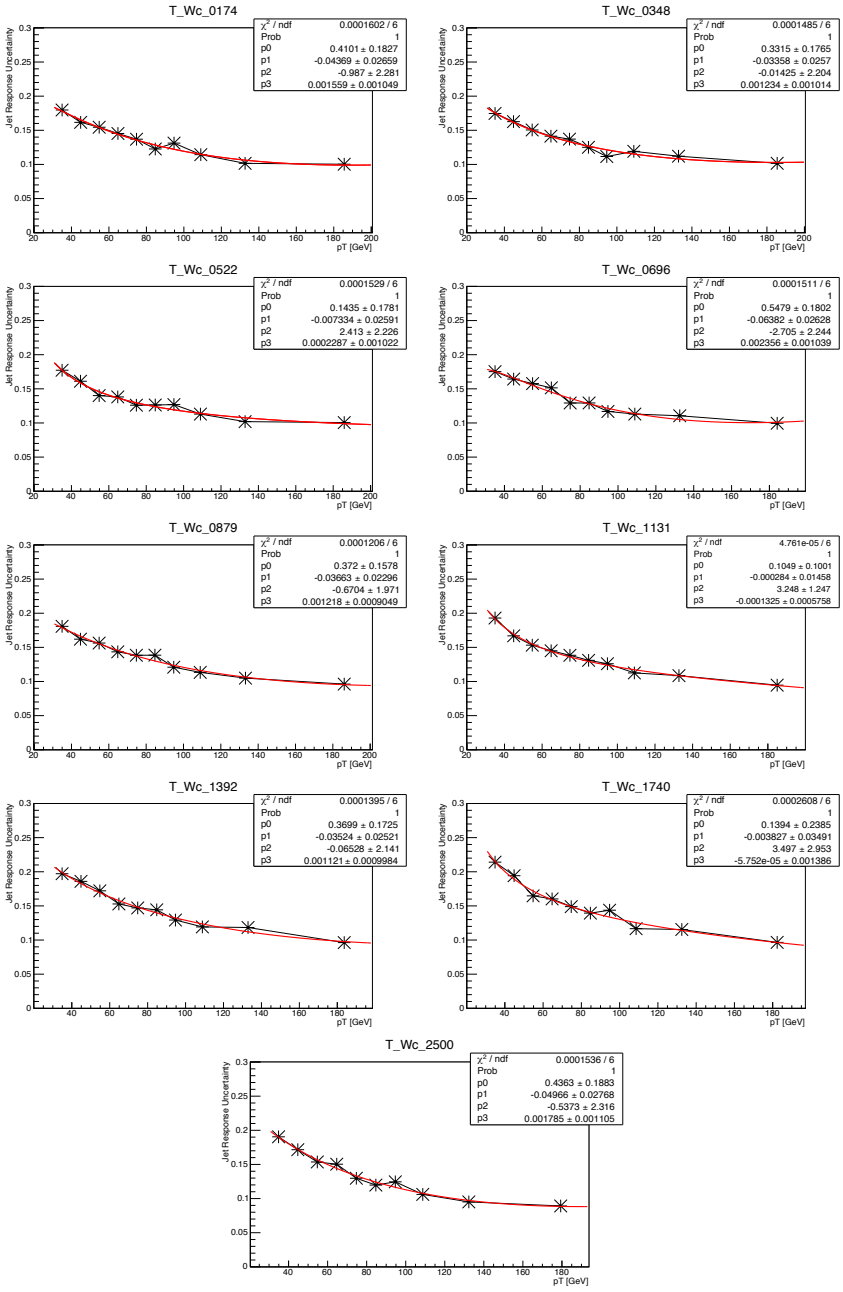

Figure A.5: Parameter fitting of correction uncertainty of c-quark jet with a function of pT in each η region

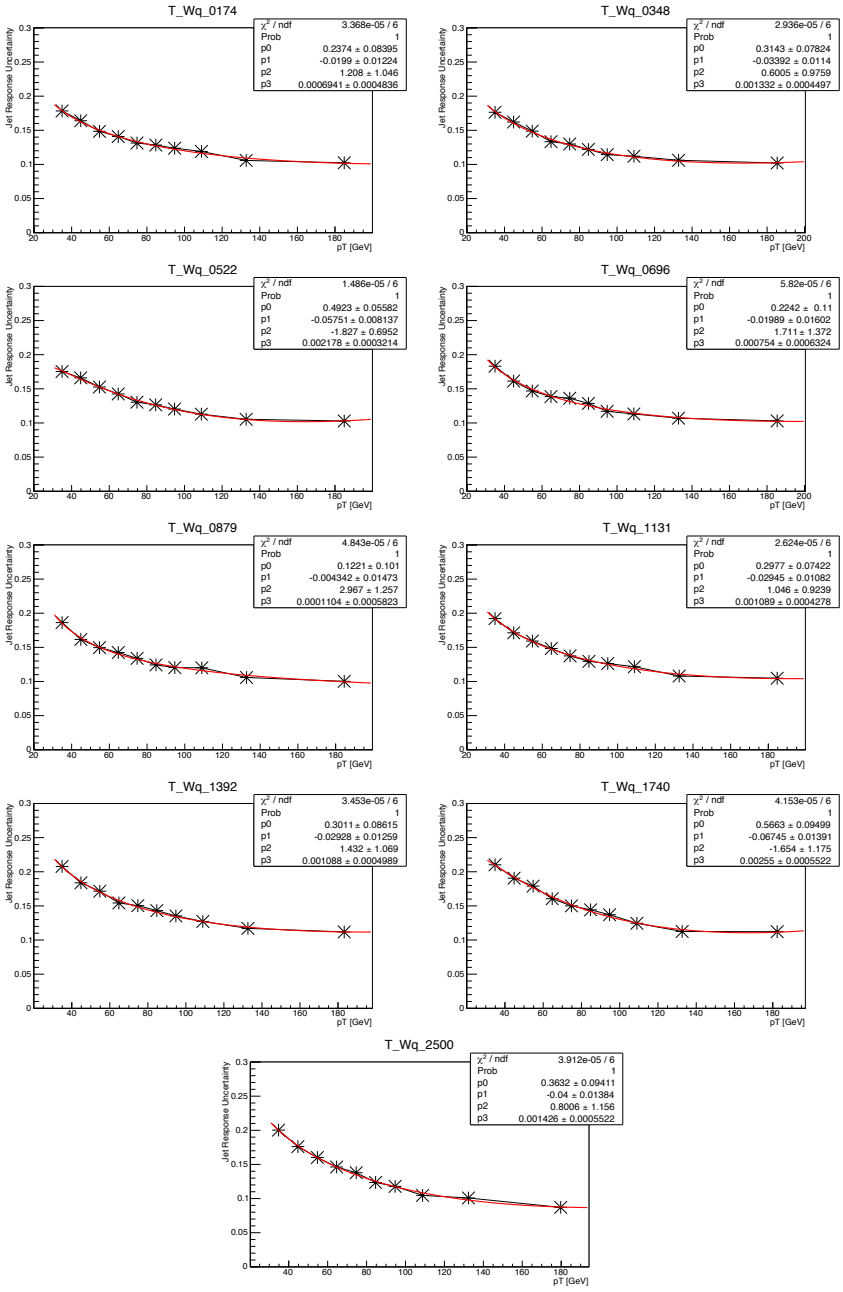

Figure A.6: Parameter fitting of correction uncertainty of light-flavour jet with a function of pT in each η region

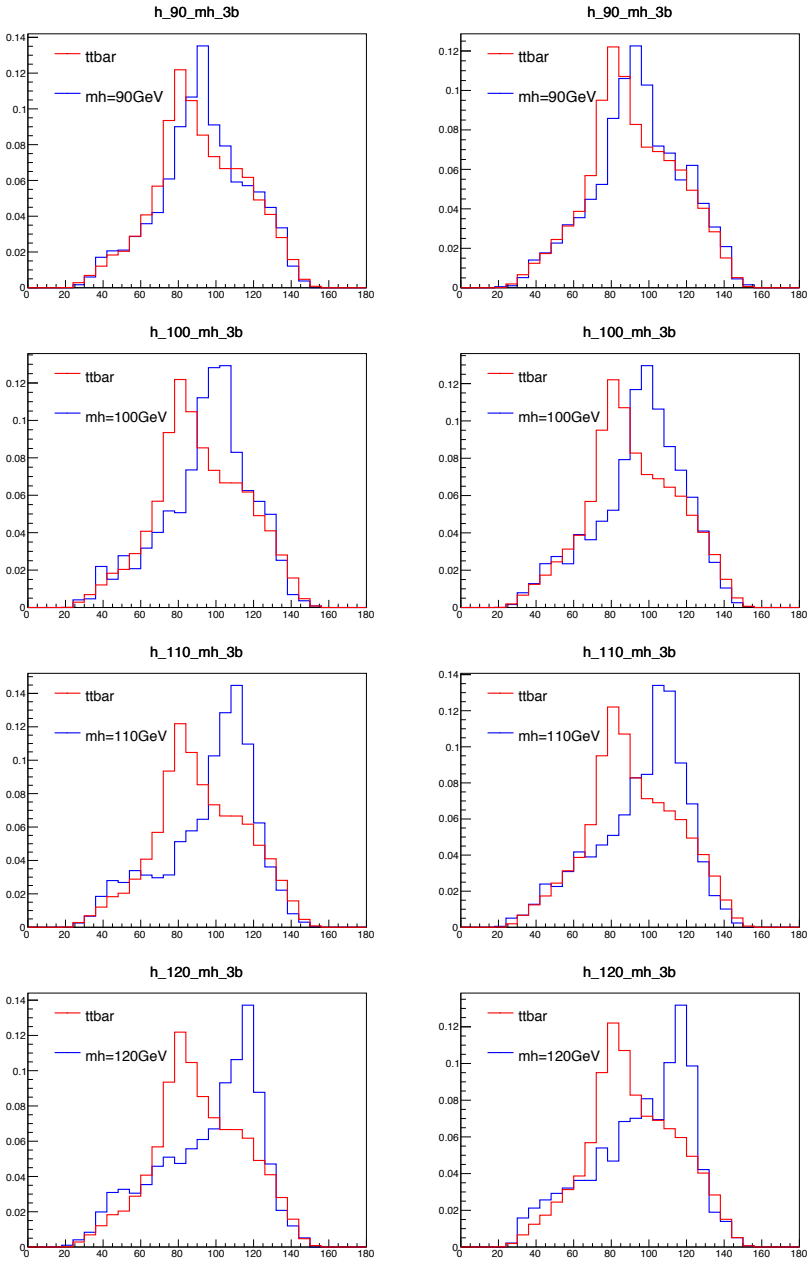

Figure A.7: Low Mass Templates in 3b-tags: $H^{\pm}$ vs W for $H^{\pm}$ mass of 90 to 120 GeV/c^2 with a normalization to unity. Template for e+jets on left and μ+jets on right side.

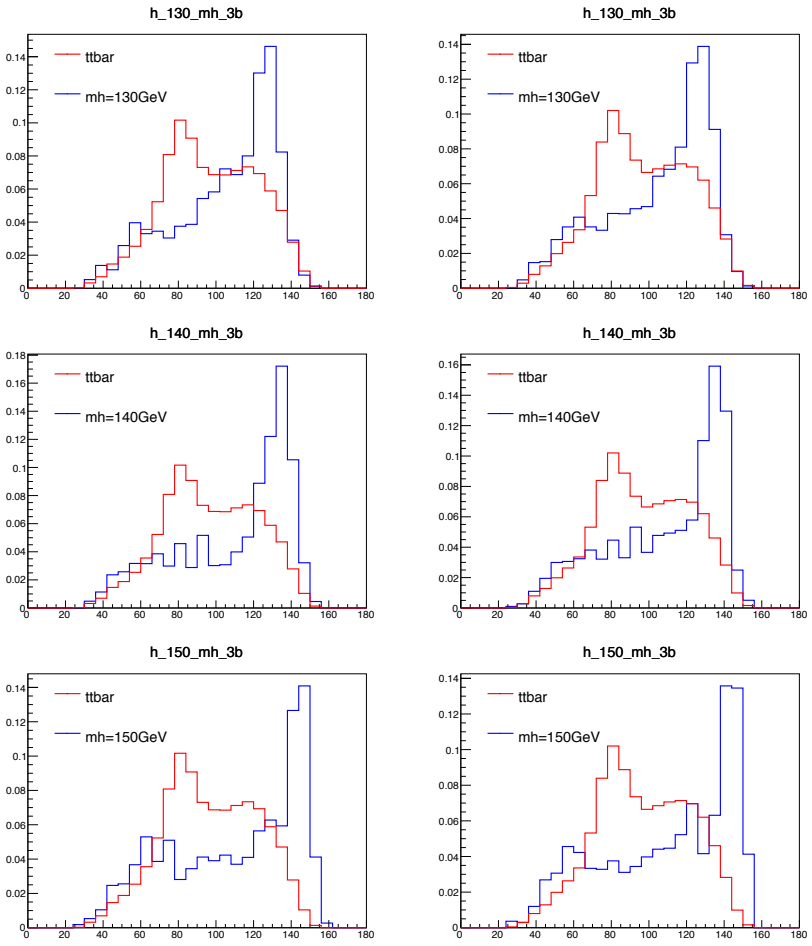

Figure A.8: High Mass Templates in 3b-tags: $H^{\pm}$ vs W for $H^{\pm}$ mass of 130 to 150 GeV/c^2 with a normalization to unity. Template for e+jets on left and μ+jets on right side.

국문 초록

이 연구는 charged Higgs 입자의 $c\bar{b}$ 붕괴 모드를 찾는 최초의 시도이다. 연구에 사용된 데이터는 CMS 실험의 19.7 fb^{-1}에 해당하는 8 TeV 에너지의 양성자 충돌에서 나온 이벤트이다. 탑쿼크의 쌍생성에서 한 쪽의 탑쿼크가 바텀쿼크와 두 개의 렙톤, 다른 쪽의 탑쿼크가 바텀쿼크와 두 개의 쿼크로 붕괴하는 경우, 두 개의 바텀쿼크로부터의 b-jet과 두 개의 light-jet, 하나의 뮤온 또는 전자, 중성미자에 의한 missing transverse energy가 최종적으로 생길 것이다. 한편, charged Higgs 입자가 두 개의 쿼크로 붕괴하는 W보존의 자리에 들어와서 $c\bar{b}$로 붕괴한다면, 최종적으로 하나의 b-jet이 더 나타날 것으로 생각되어진다. 선정된 이벤트들은 탑쿼크와, 두 개의 렙톤으로 붕괴하는 W보존의 질량을 통제한 kinematic fitter를 통하여 재구성되었고, di-jet(두 개의 jet의 벡터합)의 질량분포가 이를 통하여 얻어졌다. 이 때, di-jet의 질량분포는 표준모형의 탑쿼크 쌍생성에서는 W보존의 질량분포가 될 것이다. 이 연구에서는 di-jet 질량분포를 2개의 b-jet이 있는 경우와 3개의 b-jet이 있는 경우에 대해서 동시에 fitting을 하여, 표준모형 이상의 시그널을 찾을 수 있는지 살펴보았다. 이를 통해 탑쿼크가 charged Higgs와 바텀쿼크로 붕괴하는 분기비의 예상상한을 95%의 신뢰도로 구할 수 있었고, 이는 charged Higgs 입자의 질량 90에서 150GeV 사이에서 1% 근처로 나타났다.

주요어: Charged Higgs, Two Higgs Doublet Models, Multi Higgs Doublet Models
학번: 2014-21375